

A comparative analysis of opto-thermal figures of merit for high temperature solar thermal absorber coatings

Simon Caron^{a,*}, Jorge Garrido^b, Jesus Ballestrín^c, Florian Sutter^a, Marc Röger^a, Francisco Manzano-Agugliaro^d

^a Institute of Solar Research, German Aerospace Center (DLR), Paseo de Almería 73-2, 04001, Almería, Spain

^b Department of Energy Technology, KTH Royal Institute of Technology, SE 10044, Stockholm, Sweden

^c CIEMAT, Plataforma Solar de Almería, Carretera de Senés Km. 4.5, Tabernas, 04200, Spain

^d Department of Engineering, CEIA3, University of Almería, 04120, Almería, Spain

ARTICLE INFO

Keywords:

Concentrated solar power
Absorber coating
Solar absorptance
Thermal emittance
Spectral selectivity
Thermal efficiency

ABSTRACT

Solar thermal absorber coatings play a key role in the thermal efficiency of receivers for applications in the field of Concentrated Solar Power (CSP). The development of stable spectral selective coatings with a high solar absorptance α_{sol} and a low thermal emittance ϵ_{th} is often desired to reduce thermal losses. However, quantitative indicators describing selectivity and the trade-off between solar absorptance and thermal emittance is seldom discussed in the literature.

In this review, relevant opto-thermal figures of merit are analyzed for the comparison of reference solar thermal absorber coatings, including real and ideal coatings, both black and spectral selective. The comparison is made for a temperature ranging from 25 to 1000 °C and for a concentration factor ranging from 20 to 1000, based on spectral data measured at room temperature from 0.25 to 20 μm .

New figures of merit are introduced, i.e. a normalized selectivity ratio Si^* , a trade-off factor $Z_{\text{trade-off}}$, a normalized solar reflectance index SRI^* and a peak efficiency temperature $T_{\text{peak,opt}}$. These metrics are derived from existing figures of merit and adapted for CSP.

The set of figures of merit analyzed in this review offer a complementary perspective for the detailed characterization of any coating opto-thermal performance. For solar thermal absorber coatings, thermal efficiency η_{thermal} and peak efficiency temperature $T_{\text{peak,opt}}$ are respectively deemed more insightful than opto-thermal efficiency $\eta_{\text{opt-th}}$ and maximum steady-state temperature $T_{\text{SST,max}}$, when comparing the relative opto-thermal performance of two coating formulations.

1. Introduction

Concentrated solar radiation can be harnessed and converted into electrical power by different technologies. Direct conversion can be achieved by Concentrated Photovoltaics (CPV) [1,2] or Solar Thermoelectric Generators (STEG) [3–5]. Alternatively, conventional thermodynamic power cycles can be driven by the heat generated with Concentrated Solar Thermal (CST) systems, such as Parabolic Trough Collectors (PTC) [6–8] Linear Fresnel Collectors [9,10], Central Receiver Systems CRS [11–14] or dish concentrators [15,16]. Hybrid solar concentrators also exist, for example taking advantage of spectral beam-splitting devices, to focus solar radiation on multiple receiver types and thus increase further the conversion efficiency [17–19].

These concentrating systems consist of optical concentrators tracking the sun and focusing Direct Normal Irradiance (DNI) onto a receiver. Increasing the concentration factor C_x allows miniaturizing PV cells, at the cost of parasitic losses for device cooling [20,21]. For solar thermal processes, increasing the concentration factor allows reaching higher operating temperature levels, while miniaturizing the thermal receiver and consequently reducing heat losses, thus improving the thermodynamic efficiency. Today, CST power plants, in particular parabolic troughs (PTC) and solar towers (CRS), have achieved technical maturity for commercial systems [22]. The integration of molten salt thermal storage tanks allows a cost-efficient and dispatchable power generation [23].

Solar thermal receivers are one of the most critical components of CST power plants. Commercial PTC and CRS power plants, illustrated in

* Corresponding author.

E-mail address: simon.caron@dlr.de (S. Caron).

<https://doi.org/10.1016/j.rser.2021.111818>

Received 19 May 2021; Received in revised form 12 October 2021; Accepted 24 October 2021

Available online 9 November 2021

1364-0321/© 2021 The Authors. Published by Elsevier Ltd. This is an open access article under the CC BY license (<http://creativecommons.org/licenses/by/4.0/>).

Nomenclature**Abbreviations**

AFD	Allowable Flux Density
AM	Air Mass
BSI	Blackbody Spectral Irradiance
CERMET	Ceramic Metallic
CNT	Carbon Nanotube
CPV	Concentrated Photovoltaics
CST	Concentrated Solar Thermal
CRS	Central Receiver System
DNI	Direct Normal Irradiance
FoM	Figure of Merit
FTIR	Fourier Transform Infrared
HTF	Heat Transfer Fluid
HSA	High Solar Absorptance
IR	Infrared
LCOC	Levelized Cost of Coating
LWIR	Long Wave Infrared
NIST	U.S. National Institute of Standards and Technology
OD	Outer Diameter
PTC	Parabolic Trough Collector
PTR	Parabolic Trough Receiver
PVD	Physical Vacuum Deposition
RMSE	Root Mean Square Error
SDHR	Spectral Directional Hemispherical Reflectance
SMARTS	Simple Model for Atmospheric Transmission of Sunshine
STAC	Solar Thermal Absorber Coating
STEG	Solar Thermal Electric Generator
SSC	Spectral Selective Coating
SSI	Solar Spectral Irradiance
SST	Steady-State Temperature
TBC	Thermal Barrier Coating
UHI	Urban Heat Island

English Symbols

C_x	Concentration ratio (Suns)
Cr	Convection to radiation heat transfer adimensional number (—)

f_{SSC}	Spectral selective coating model (—)
f_{shape}	Spectral shape factor (—)
f_{Carnot}	Fraction of Carnot Efficiency (%)
F_{view}	View factor (—)
E_{bb}	Blackbody spectral Irradiance ($W.m^{-2}.\mu m^{-1}$)
G_{sol}	Solar spectral Irradiance ($W.m^{-2}.\mu m^{-1}$)
h_{rad}	Radiation heat transfer coefficient ($W.m^{-2}.K^{-1}$)
h_{conv}	Convection heat transfer coefficient ($W.m^{-2}.K^{-1}$)
$k_{coating}$	Coating thermal conductivity ($W.m^{-1}.K^{-1}$)
k_{metal}	Metal thermal conductivity ($W.m^{-1}.K^{-1}$)
p.p.	Percentage point (%)
q''_{use}	Useful heat flux ($W.m^{-2}$)
q''_{sol}	Concentrated solar flux ($W.m^{-2}$)
$q''_{rad,sky}$	Radiation heat flux ($W.m^{-2}$)
$q''_{conv,amb}$	Convection heat flux to ambient ($W.m^{-2}$)
q''_{cond}	Conduction heat flux ($W.m^{-2}$)
$q''_{conv,HTF}$	Convection heat flux to heat transfer fluid ($W.m^{-2}$)
Si	Selectivity index (—)
Si^*	Normalized Selectivity index (—)
T_{abs}	Absorber surface temperature (K)
T_{amb}	Ambient temperature (K)
T_{sky}	Sky temperature (K)
$T_{SST,max}$	Maximum steady-state temperature (K)
SRI	Solar Reflectance Index (—)
SRI^*	Normalized Solar Reflectance Index (%)
$Z_{trade-off}$	Trade-off factor (—)

Greek Symbols

α_{sol}	solar absorptance (%)
ε_{th}	thermal emittance (%)
Δ	Difference (—)
λ	wavelength (μm)
$\lambda_{cut-off}$	cut-off wavelength (μm)
$\eta_{coating}$	Coating opto-thermal efficiency (%)
$\eta_{thermal}$	Thermal efficiency (%)
ρ	Reflectance (%)
θ	Incidence angle ($^\circ$)

Fig. 1. use tubular receiver designs. A Parabolic Trough Receiver (PTR) consists of an absorber tube inserted into an evacuated glass envelope [24,25]. External tubular receivers mounted in CRS consist of several panels of parallel absorber tubes [26,27]. In both receiver configurations, the absorber tube is made of a metal substrate, for instance a stainless steel or a nickel-based alloy, on which a Solar Thermal Absorber Coating (STAC) is applied.

Different STAC formulations are applied in state-of the art commercial PTC and CRS power plants: Spectral Selective Coatings (SSC) are typical for PTRs [28,29] while non-selective, High Solar Absorptance

(HSA) coatings are preferred for CRS [30–32]. A SSC is characterized by a high solar absorptance α_{sol} and a low thermal emittance ε_{th} , while a HSA black coating only exhibits a high α_{sol} value (>95%). Several considerations drive the selection of a coating, beside its opto-thermal performance: i) the heat transfer fluid (HTF) operating temperature range [33,34], ii) the coating durability in operating conditions [35–37] and iii) the Levelized Cost of Coating (LCOC) [38,39]. These design considerations are outlined in Table 1 and briefly discussed further.

For PTC systems, Diphenyl Oxide/Biphenyl based thermal oils are the current state-of the art HTF [40,41], operating from 290 at the inlet

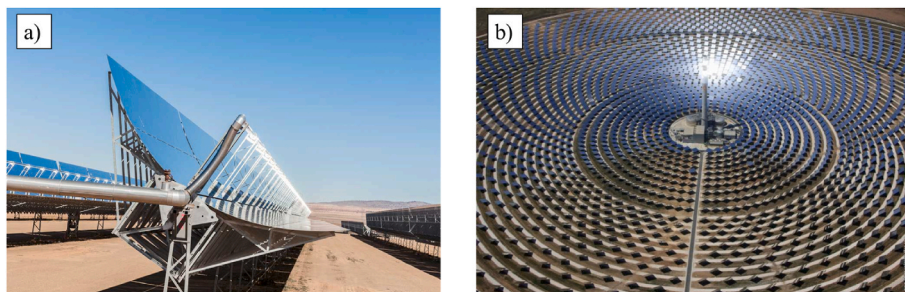


Fig. 1. Illustration of PTC and CRS technologies. a) Parabolic Trough Concentrator (Andasol-3, Spain) [80]. b) Central Receiver System (Gemastar, Spain) [81].

Table 1

Summary of boundary conditions for PTC and CRS applications relevant for STAC selection.

Parameter	Parabolic Trough Collector (PTC)	Central Receiver System (CRS)
Concentration factor C_x	Constant, $\sim x20 \dots x100$ [6–8]	Variable, $x100 \dots x1000$ [11–14]
Solar field aperture area (m^2)	500,000 m^2 /50 MWe [82]	300,000 m^2 /20 MWe [81]
HTF operating temperature range ($^{\circ}C$)	<i>Thermal oils:</i> 290–425 $^{\circ}C$ [33, 40–43] <i>Molten nitrate salts:</i> 270–600 $^{\circ}C$ [33, 44, 45]	<i>Molten nitrate salts:</i> 270–600 $^{\circ}C$ [33, 44, 45] <i>Liquid sodium:</i> 100–800 $^{\circ}C$ [33, 34, 49, 50]
Receiver and absorber geometrical dimensions	<i>Parabolic trough receiver:</i> “Standard” dimensions [24, 25] Receiver height above ground: < 5 m Absorber tube diameter: 70 mm Receiver length: 4 m	<i>External tubular receiver:</i> Custom dimensions [26, 27, 72–76] Tower height: $\sim 100 \dots 250$ m Receiver height: $\sim 10 \dots 20$ m Receiver diameter: $\sim 10 \dots 20$ m
Industrial production scale	<i>Standardized design, large series</i> >20,000 PTR units for a 50 MWe PTC solar thermal power plant [82]	<i>Custom design, small series</i> ~ 20 receiver panels per tower $\sim x50$ tubes per receiver panel [26, 27, 72–76]
STAC formulation and application process	Thin film multilayered SSC (CERMET) PVD or sol-gel dip coating [28, 29, 64–68]	Silicon based ceramic black paint Thermal spraying technique [30–32, 37, 61–63]
Atmospheric conditions and STAC maintenance/durability	Vacuum sealed, maintenance free Stable in vacuum, oxidation in air [35, 56–59]	Atmospheric pressure (air) re-coating allowed on site [36–39, 60]
STAC service lifetime	≥ 25 years [35, 56–59]	5–10 years [36–39, 60]

up to 390 $^{\circ}C$ at the outlet of a PTC loop, while new silicone oils currently operate up to 430 $^{\circ}C$ [42, 43]. Next generation power plants consider molten nitrate salts as a HTF, shifting the maximum operating temperature range toward 600 $^{\circ}C$ [44, 45]. In the case of CRS, molten salts are currently a state-of the art HTF. Next generation CRS power plants consider new HTF formulations [46], for instance new ternary molten salt mixtures [47, 48], liquid sodium [34, 49, 50] or solid particles [51–55] as a HTF to achieve a higher outlet temperature, toward 1000 $^{\circ}C$. STAC formulations for PTC applications are thus typically designed for a maximum operating temperature of 600 $^{\circ}C$ in vacuum, while these formulations are designed to withstand an operating temperature above 600 $^{\circ}C$ in air for CRS applications.

The receiver assembly and its durability are further parameters to consider when selecting a STAC formulation. PTR absorber tubes are typically sealed in vacuum [56]. The vacuum is designed to remain stable in the field over the receiver lifetime [57]. This vacuum improves the receiver thermal efficiency by canceling convection losses, but it also protects the STAC from high temperature oxidation. The glass envelope protects the STAC from environmental stresses, such as sandstorms. In case of a vacuum loss, the STAC performance may remain stable in air up to the maximum operating temperature [58]. For CRS, the receiver is mounted on top of a tower at a height typically above 100 m in desert environments. STAC are exposed in air to higher operating temperatures, oxidation and corrosion, as well as further environmental stresses. In case of degradation, defect absorber coatings in PTRs cannot be replaced, but single receivers can be replaced in the worst case [59]. For CRS, a periodical recoating could be performed on site [36–39, 60], while current research tries to identify more efficient and durable STAC formulations [61–63].

For each CSP technology, a different coating process is applied. For PTR systems, industrial grade SSC formulations are typically applied using Physical Vacuum Deposition (PVD) or sol-gel dip-coating techniques [29, 35, 64, 65], which are cost-efficient in large series production. One typical SSC architecture is a multilayered thin film coating (less than 1 μm) applied on a polished metal substrate, consisting of an infrared (IR) layer, a composite absorbing ceramic-metallic (CERMET) layer and a top antireflection (AR) layer, with intermediate diffusion barrier layers to improve further thermal stability [66–68]. For CRS, industrial grade black coatings are typically applied by spraying techniques in the workshop or on site for tubular absorber panels. These coatings are typically silicon-based ceramic paint formulations including black spinel pigments [31, 32, 37, 61–63]. Such coatings may require a thermal treatment (curing) in custom muffle furnaces or directly on site. These coatings have a thickness of ~ 30 –50 μm and can be applied as a single layer or combined with a primer coating.

Finally, an accurate online monitoring of the absorber temperature is also a critical part of plant operation, which may also be affected by the STAC choice. In PTR, the HTF inlet and outlet temperatures are measured and controlled in real time with built-in temperature sensors. The absorber surface temperature T_{abs} does not have to be monitored in real time, as the concentration factor C_x remains nearly constant. The glass envelope temperature can be monitored periodically with ground based or airborne LWIR (8–14 μm) cameras to detect partial vacuum loss [52, 69–72].

In CRS, the HTF loop temperature is also monitored in real time with a similar instrumentation. Online temperature monitoring is particularly critical for molten salts, to avoid HTF freezing below 300 $^{\circ}C$ and pronounced corrosion around 600 $^{\circ}C$ [44, 45]. To comply with these constraints, a dynamic heliostat field aiming strategy allows defining a variable concentration factor and an “Allowable Flux Density” (AFD) on the receiver surface [73–76]. In order to avoid local overheating, the absorber surface temperature T_{abs} has to be monitored in real time with ground mounted LWIR cameras (8–14 μm) to optimize the heliostat field aiming strategy [77, 78]. These cameras are nearly “solar blind” in this spectral range if the absorber coating is similar to a blackbody [79].

Today, there are two main research paths in the field of coating development for CRS applications, i.e. the development of stable high temperature SSC and HSA coatings. Two standard opto-thermal figures of Merit (FoM) are the solar absorptance α_{sol} and thermal emittance ϵ_{th} [83–92]. The selection of a research path is driven by a ranking and trade-off between these reference FoMs: Is it rather worth selecting a high temperature “space” black coating to maximize the α_{sol} value towards 100%, or selecting a high temperature SSC instead, with a high α_{sol} and a low ϵ_{th} values? In addition to these reference FoMs, further FoMs have been previously reported in the literature to compare the performance of different STAC formulations:

- Selectivity ratio $\alpha_{sol}/\epsilon_{th}$ [92, 93]
- Selective coating spectral parameters, i.e. shape factor f_{shape} , cut-off wavelength $\lambda_{cut-off}$ [94, 95]
- The useful heat gained by the STAC \dot{q}_{use}'' [96, 97].
- The coating opto-thermal efficiency η_{opt-th} [11–13, 30, 38, 39]
- The trade-off factor between α_{sol} and ϵ_{th} [30, 98]
- The “stagnation” temperature $T_{SST, max}$ [92, 99]
- The receiver thermal efficiency $\eta_{thermal}$ [11, 12, 96, 97]
- The Solar Reflectance Index SRI [87–89, 100, 101].

The aim of this paper is to provide a comparative analysis of FoMs outlined above, relevant for characterizing the performance of high temperature STAC. These FoMs are calculated on the basis of spectral data measured at room temperature for reference coatings. The respective influence of solar concentration C_x and absorber surface temperature T_{abs} are highlighted where relevant. FoM equations are introduced and re-normalized, if necessary. Section 2 presents a

framework describing the system definition, reference coatings. In Section 3, FoM equations are defined and reviewed. FoM values are calculated for reference coatings and analyzed in Section 4. .

2. Materials and methods

2.1. System definition

A heat flux diagram is sketched in Fig. 2 for CST systems and for a high temperature STAC applied on a metal substrate. The Direct Normal Irradiance (DNI) is specularly reflected by tracking mirrors and transmitted through the atmosphere toward the receiver surface. The DNI is concentrated by a optical concentration factor C_x . The STAC absorbs a fraction α_{sol} of the concentrated solar flux \dot{q}_{sol}'' , which heats up the STAC to a surface temperature T_{abs} . The complementary fraction $(1 - \alpha_{sol})$ is reflected to the ambient. The STAC loses heat by radiation ($\dot{q}_{rad,sky}''$) toward the sky and by convection ($\dot{q}_{conv,amb}''$) to the ambient.

The net heat flux balance is written in (Eq. (1)), defining the useful heat flux \dot{q}_{use}'' . This heat flux is transferred by conduction (\dot{q}_{cond}'') through the coating and metal substrate, inducing a first temperature drop at the interface between coating and metal ($\Delta T_{coating}$) and another temperature drop at the interface between metal and fluid (ΔT_{metal}) (Eq. (2)). According to Fourier's law, these temperature drops are proportional to the respective thermal conductivities ($k_{coating}$, k_{metal}) and thicknesses. The useful heat flux is then transferred by convection to the HTF (Eq. (3)).

$$\dot{q}_{use}'' = \alpha_{sol} \dot{q}_{sol}'' - \dot{q}_{rad,sky}'' - \dot{q}_{conv,amb}'' \quad (1)$$

$$\Delta T = \Delta T_{coating} + \Delta T_{metal} \quad (2)$$

$$\dot{q}_{use}'' = \dot{q}_{cond}'' = \dot{q}_{conv,HTF}'' \quad (3)$$

2.2. Modelling assumptions

In order to compare the performance of different STAC for a wide range of applications, further calculations are performed using the following set of assumptions for simplification:

- a) The atmosphere is not attenuating the radiation transfer between mirrors and the receiver.

- b) The mirror is perfectly specular and it exhibits an ideal spectral reflectance, i.e. it reflects 100% of solar DNI from 0.28 to 2.5 μm . Beyond this wavelength, the reflectance is negligible.
- c) The incidence angle θ of DNI onto the mirror surface is nearly normal ($\theta \sim 10^\circ$)
- d) The incidence angle θ of concentrated irradiance onto the receiver surface is nearly normal.
- e) The concentrated solar flux \dot{q}_{sol}'' is homogeneous on the receiver surface.
- f) The ambient and sky temperature are equal ($T_{amb} = T_{sky}$) and set to 25 $^\circ\text{C}$.
- g) The convection heat loss from the STAC to the ambient is neglected ($\dot{q}_{conv,amb}''$)
- h) The receiver is not covered by any glass envelope.
- i) The receiver geometry is flat.
- j) The view factor F_{view} to the surroundings is equal to 1.
- k) The STAC is lambertian, i.e. it is a diffusely reflecting surface.
- l) The STAC is opaque, i.e. its transmittance is null.
- m) The STAC is isothermal and adiabatically insulated.

This set of assumptions is obviously ideal, in order to focus on a STAC opto-thermal performance instead of other secondary variables. The validity of these assumptions is briefly discussed in Table 2 for PTC and CRS applications, including relevant references. The heat transfer from the STAC to the HTF is not modelled in this paper.

2.3. Reference coatings

For the comparative analysis, four reference STAC are defined: i) a reference SSC, ii) an ideal SSC with a sharp cut-off wavelength at 2.5 μm , iii) a reference black coating, iv) an ideal blackbody coating. Their spectral directional hemispherical reflectance (SDHR) ρ_{SDHR} are plotted in Fig. 3.

The SDHR has been measured [86] at OMT Solutions BV optical laboratory in the Netherlands [114], at room temperature, with two complementary spectrophotometers, for a near normal incidence angle θ of 10° . The SDHR is measured from 0.25 to 2.5 μm with an ultra-violet-visible-near infrared (UV-VIS-NIR) spectrophotometer, using a NIST traceable white diffuse sintered PTFE standard (e.g. Spectralon® [115]). The SDHR is then measured from 1.6 to 20 μm with a Fourier Transform Infrared (FTIR) spectrophotometer, using a NIST traceable specular gold standard (e.g., Infragold®, [115]). A consistent spectral

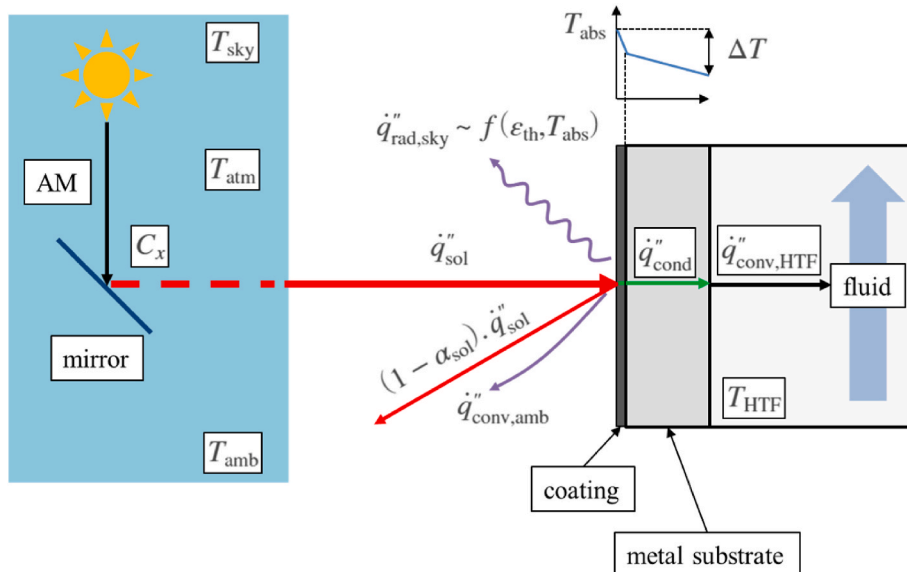


Fig. 2. Heat flux diagram for a high temperature STAC.

Table 2

Validity and limitations of modelling assumptions for PTC and CRS applications.

Assumption	Parabolic Trough Collector (PTC)	Central Receiver System (CRS)
a) Atmospheric attenuation between mirrors and receiver	Short range (<10 m) Assumption valid	Medium range (100 m ... 1 km); Assumption not valid [102–104]
b) Ideal mirror specular solar reflectance [0.28–2.5] μm	Ideal assumption for clean second surface glass silvered mirrors (solar weighted hemispherical reflectance >95%) [105–107]	
c) Near normal incidence angle of DNI onto mirrors	Variable incidence on one axis tracking parabolic mirrors [7,95,108]	Variable incidence angle on two axis tracking heliostats [13,14,108]
d) Near normal incidence of irradiance onto receiver	Variable incidence on tubular receiver [7,95]	Variable incidence on receiver surface due to aiming strategy [109]
e) Homogeneous concentrated solar flux q''_{sol}	Assumption approximately valid, circumferential variations [7,95]	Assumption not valid, variable flux due to heliostat field layout dynamic aiming strategy [72–76]
f) Isothermal ambient and sky temperatures ($T_{amb} = T_{sky}$)	Assumption only valid under laboratory room; PTR facing mirror and sky [24,25,56,71]	Assumption only valid under laboratory conditions; Receiver vertically mounted [26, 27]
g) Negligible convection from STAC to ambient	Assumption valid for an evacuated receiver tube [7,24,25,56,57,69–71]	Assumption not valid, convection losses cannot be neglected at tower height [26,110]
h) Receiver without glass cover	Assumption not valid, concentric glass envelope [24,25]	Valid assumption [26, 27]
i) Flat receiver geometry	Assumption not valid (Diameter: ≥ 70 mm) [24, 25]	Assumption not valid Variable tube diameter [72–76]
j) View factor $F_{view} = 1$	Assumption not valid, concentric glass envelope [24,25]	Assumption not valid, neighboring absorber tubes [109]
k) The STAC is lambertian	Assumption not valid, SSC is specular [111]	Assumption nearly valid for a diffuse black paint [111,112]
l) The STAC is opaque	Assumption not valid for a thin film STAC with multiple layers [28,29, 66–68]	Assumption valid for a micrometric black coating [30–32,37, 61–63,98]
m) The STAC is isothermal	Assumption valid for a receiver section, thin film SSC with high thermal conductivity [113]	Assumption valid for a receiver section. Thermal gradient across the black coating (few μm thick, with low thermal conductivity) [31]

overlap is observed in the range from 1.6 to 2.5 μm , with an average residual mismatch smaller than 2% points (p.p.).

Reference SSC and HSA flat samples are shown in Fig. 4 along with bare and coated tubular samples. Similar samples have been tested within the European research project RAISELIFE [116,117] for temperature levels above 600 °C.

References spectra for ideal selective and black coatings were both modelled by a Heavyside unit step function (Eq. (4)), with respective cut-off wavelengths $\lambda_{cut-off}$ of 2.5 and 0 μm . Both reference coatings are designed to maximize α_{sol} regardless of the operating point $\{C_x, T_{abs}\}$. The reference SSC is not necessarily optimal in terms of efficiency [94, 95].

$$\rho_{SDHR,ideal}(\lambda) = \begin{cases} 0; & \lambda \leq \lambda_{cut-off} \\ 1; & \lambda > \lambda_{cut-off} \end{cases} \quad (4)$$

A few assumptions are made regarding coating spectral properties in subsequent calculations. First, it is assumed that these reference coatings are thermally stable for any temperature, i.e. ρ_{SDHR} remains constant

before and after isothermal exposure and does not age. Furthermore, it is assumed that ρ_{SDHR} is not temperature dependent (Eq. (5)), i.e. the SDHR does not shift when the sample is heated up. Previous research has shown that this assumption is not necessarily valid, requiring more sophisticated instrumentation to measure SDHR at operating temperature [90,91,118–123].

$$\frac{d\rho_{SDHR}(\lambda, \theta, T_{abs})}{dT_{abs}} \rightarrow 0 \quad (5)$$

2.4. Inventory of FoMs

A list of relevant opto-thermal FoMs for the characterization of STAC performance has been outlined in Section 1. A synoptical diagram is shown in Fig. 5 to illustrate interactions between FoMs. Their equations are developed in the next subsections.

The synoptical diagram shown in Fig. 5 is split into four levels, sorting FoMs by increasing level of complexity. Spectra are listed on the top level as inputs for the calculation process. Spectral data include coating SDHR (Fig. 3), Solar Spectral Irradiance (Fig. 5), Blackbody Spectral Irradiance (Fig. 6). Information about the operating conditions $\{C_x, T_{abs}\}$ are also relevant.

The first level includes elementary FoMs, i.e. the SSC model, the solar absorptance as a function of air mass, α_{sol} (AM) and the thermal emittance as a function of absorber temperature, ϵ_{th} (T_{abs}). The second level includes compound FoMs, i.e. Selectivity ratios (S_i, S_i^*), the useful heat flux q''_{use} , the opto-thermal efficiency η_{opt-th} and the trade-off factor $Z_{trade-off}$. Third level FoMs are built from Level 2 FoMs, introducing reference “cold” and “hot” temperatures. These FoMs are the maximum steady-state temperature $T_{SST,max}$, solar reflectance indices (SRI, SRI*), the receiver thermal efficiency $\eta_{thermal}$ and the peak efficiency temperature $T_{peak,opt}$.

Relevant FoMs for the comparative analysis of STAC performance are listed in Table 3 with their respective symbols, units, input variables, targets for STAC and ranges.

3. Definition of FoMs

3.1. Level 1 FoMs

3.1.1. Solar absorptance

Solar absorptance α_{sol} is a standard FoM for STAC [83,86,87]. The formula is expressed in (Eq. (6)):

$$\alpha_{sol}(AM) = \frac{\int_{\lambda_1}^{\lambda_2} [1 - \rho_{SDHR}(\lambda, \theta, T_{amb})] G_{sol}(\lambda, AM) d\lambda}{\int_{\lambda_1}^{\lambda_2} G_{sol}(\lambda, AM) d\lambda} \quad (6)$$

Where $G_{sol}(\lambda, AM)$ is the solar spectral irradiance expressed in $\text{W}\cdot\text{m}^{-2}\cdot\mu\text{m}^{-1}$ for a given Air Mass AM, $\rho_{SDHR}(\lambda, \theta, T_{amb})$ is the SDHR measured at near normal incidence ($\theta \sim 10^\circ$) and at ambient temperature ($T_{amb} \sim 25^\circ\text{C}$) [83,86].

The SDHR is weighted by a reference solar spectral irradiance (1 Sun, i.e. $C_x = 1$) on the wavelength range $[\lambda_1 - \lambda_2]$. In practice, calculations for CSP relevant materials are carried out with the ASTM G173-03 spectrum and reported for AM1.5, considering direct + circumsolar irradiance [124]. The wavelength interval considered for integration usually spans from $\lambda_1 = 0.28 \mu\text{m}$ to $\lambda_2 = 2.5 \mu\text{m}$. The influence of the mirror spectral specular reflectance [105] is not considered here. In this paper, the spectral resolution is set to $10^{-3} \mu\text{m}$ (1 nm).

The ASTM G173-03 is computed with SMARTS v2.9.2 [125] for the U.S. 1976 Standard Atmosphere from 0.28 to 4 μm [126–128], using the AM0 extraterrestrial spectrum derived in Ref. [129], which has been updated in Ref. [130]. The reference solar spectral irradiance data for calculation is plotted in Fig. 6 a. In this paper, the AM variable is allowed to vary between AM0 (Extraterrestrial) to AM5 to assess its influence on the solar absorptance calculation. For AM1.5 conditions (direct +

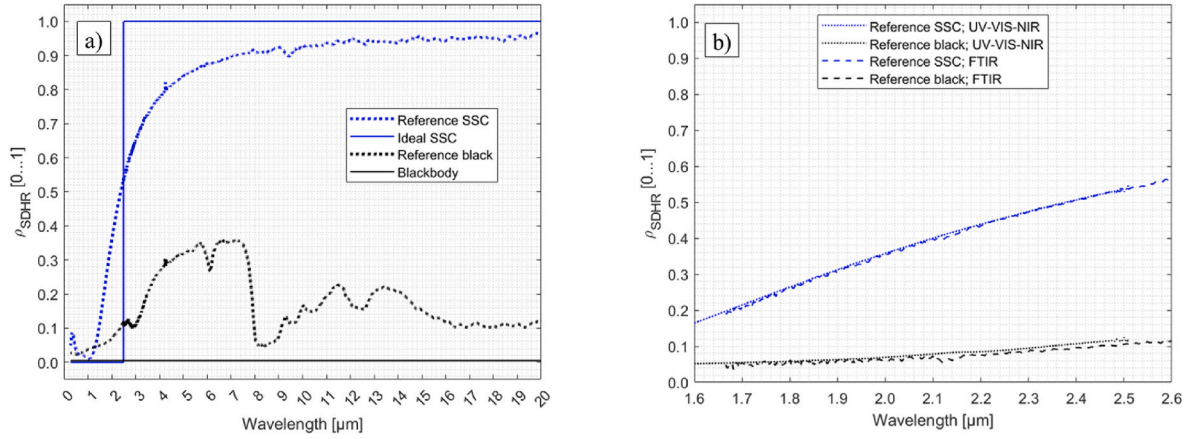


Fig. 3. Spectral directional hemispherical reflectance (SDHR) data for reference STAC. a) SDHR for reference STAC plotted from 0.28 to 20 μm . b) Spectral overlap between 1.6 and 2.5 μm for the two STAC samples measured with UV-VIS-NIR and FTIR spectrophotometers.

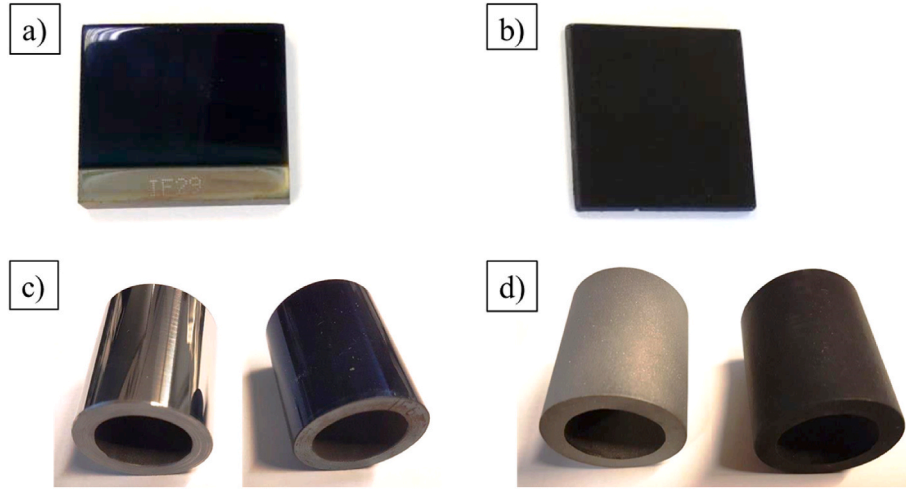


Fig. 4. Pictures of absorber coatings applied on T91 flat and tubular metal substrates. a) Flat reference sample coated with the ref. SSC b) Flat reference sample coated with the ref. HSA black coating. c) Tubular samples, bare polished substrate and coated with the ref. SSC. d) Tubular samples, bare sand blasted substrate and coated with the ref. HSA black coating.

circumsolar), the solar irradiance integrated from 0.28 to 4 μm equals 900 W m^{-2} .

The cumulative fraction of solar spectral irradiance $SSI_{\text{cum,rel}}$ is expressed in (Eq. (7)) and plotted in Fig. 6 b after normalization with respect to AM1 (1 kW/m^2). This indicator allows a better visualization of the spectral weight distribution. It also corresponds to the solar absorptance of an ideal blackbody ($\rho_{\text{SDHR}} = 0$). The AM0 curve is smooth, as the atmosphere does not hamper extraterrestrial solar irradiance. This spectrum can be reasonably approximated by a blackbody at a temperature of 5777 K [96]. As the AM value increases, the weight distribution shifts slightly toward higher wavelengths, as the solar spectrum peak shifts toward the near IR range. A few atmospheric absorption bands (0.9, 1.2, 1.4, 1.9 μm) do not contribute to the spectral weight distribution, as solar spectral irradiance is spectrally filtered by the atmosphere. An asymptotical value of 99% is reached at 2.5 μm , if $\lambda_2 = 4 \mu\text{m}$.

$$SSI_{\text{cum,rel}} = \frac{\int_{\lambda_1}^{\lambda_2} G_{\text{sol}}(\lambda, AM) d\lambda}{\int_{\lambda_1}^{\lambda_2} G_{\text{sol}}(\lambda, AM) d\lambda} \quad (7)$$

3.1.2. Thermal emittance

Thermal emittance $\varepsilon_{\text{th,calc}}$ is another standard FoM for STAC [83, 88–92]. The formula is expressed in (Eq. (8)), where $E_{\text{bb}}(\lambda, T_{\text{abs}})$ is the

blackbody spectral irradiance expressed in $\text{W.m}^{-2} \cdot \mu\text{m}^{-1}$ (Eq. (9)). The SDHR measured at room temperature is weighted by a reference blackbody spectral irradiance at an absorber temperature T_{abs} on the wavelength range $[\lambda_1 - \lambda_3]$.

$$\varepsilon_{\text{th,calc}}(T_{\text{abs}}) = \frac{\int_{\lambda_1}^{\lambda_3} [1 - \rho_{\text{SDHR}}(\lambda, \theta, T_{\text{amb}})] E_{\text{bb}}(\lambda, T_{\text{abs}}) d\lambda}{\int_{\lambda_1}^{\lambda_3} E_{\text{bb}}(\lambda, T_{\text{abs}}) d\lambda} \quad (8)$$

$$E_{\text{bb}}(\lambda, T_{\text{abs}}) = \frac{2\pi hc^2}{\lambda^5 \left[\exp\left(\frac{hc}{\lambda k T_{\text{abs}}}\right) - 1 \right]} \quad (9)$$

The wavelength interval $[\lambda_1 - \lambda_3]$ considered for integration is not consistent in the literature. Ideally, the interval range should be as wide as possible to cover the highest fraction of Stefan Boltzmann's law. In this paper, we set $\lambda_1 = 0.28 \mu\text{m}$ and $\lambda_3 = 20 \mu\text{m}$. In practice, the interval range is often limited to the FTIR spectrophotometer working range, typically from 2 to 16 μm . The start wavelength λ_1 should however match to the UV-VIS-NIR spectrophotometer, as a fraction of thermal radiation may be emitted at short wavelength (Fig. 7a). The SDHR measurement data should thus be thus concatenated, checking for the spectral mismatch in the overlap range (Fig. 3b). Another common reporting shortcoming consists in communicating a ε_{th} value only for one absorber temperature T_{abs} . The calculation should be preferably

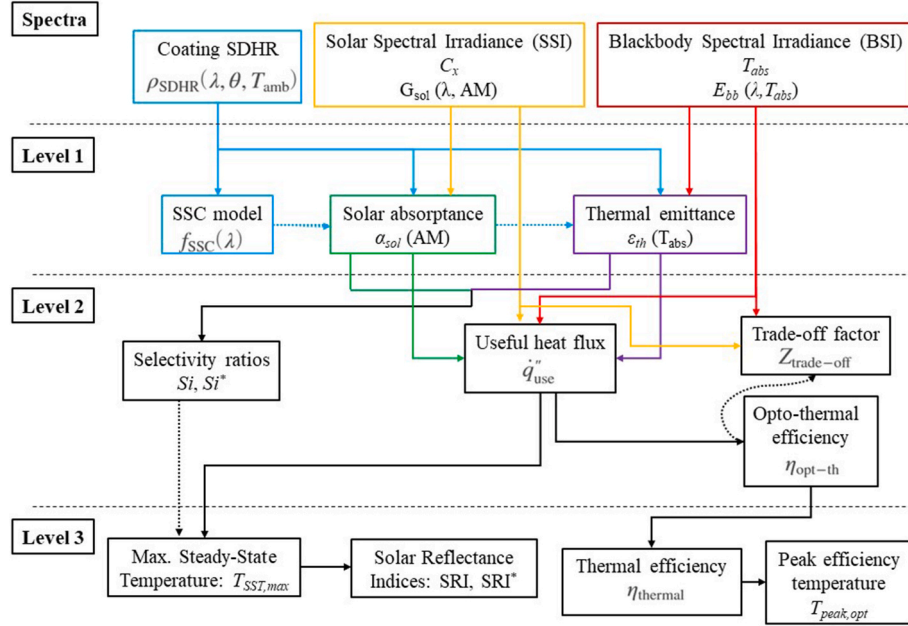
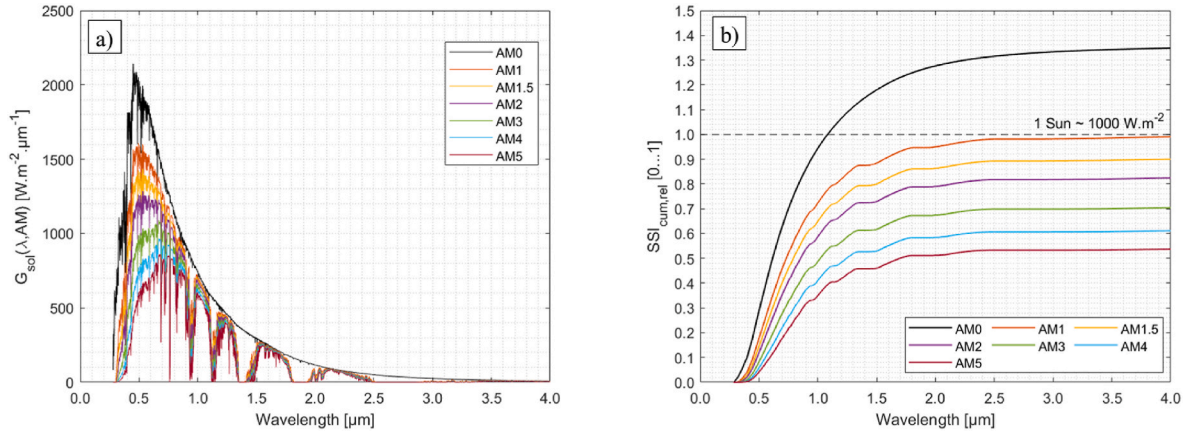


Fig. 5. Synoptical diagram of STAC opto-thermal FoMs.

Fig. 6. Reference data for Solar Spectral Irradiance. a) SSI plotted for different AM values from 0.28 to 4 μm . b) Cumulative SSI fraction normalized by 1000 W/m² (x1 sun) for different AM values.

reported over a temperature range.

The blackbody spectral irradiance $E_{bb}(\lambda, T_{abs})$ is plotted in Fig. 7 a on a semi-logarithmic plot and the cumulative fraction of blackbody spectral irradiance $BSI_{cum,rel}$ (Eq. (10)) is shown in Fig. 7 b. as a fraction of Stefan Boltzmann law ($\sigma \cdot T^4$). As T_{abs} increases, blackbody spectral irradiance peak shifts towards shorter wavelengths, accordingly to Wien's displacement law. The cumulative fraction $BSI_{cum,rel}$ below 2.5 μm thus increases for higher temperature, starting from 200 °C (Fig. 6b). The cumulative fraction $BSI_{cum,rel}$ up to 20 μm approaches Stefan's Boltzmann law as temperature increases. At 25 °C, this fraction only reaches 73.5%, while it reaches 97.9% at 600 °C.

$$BSI_{cum,rel} = \frac{\int_{\lambda_1}^{\lambda_2} E_{bb}(\lambda, T_{abs}) d\lambda}{\int_{\lambda_1}^{\lambda_3} E_{bb}(\lambda, T_{abs}) d\lambda} \quad (10)$$

It is worth observing that solar and blackbody spectral irradiances partially overlap (Fig. 8). In Fig. 8 a, the respective spectral irradiances are normalized by their maximum values, while cumulative spectral irradiances are shown in Fig. 8 b. For a high temperature STAC, the influence of this overlap on the opto-thermal performance is a function

of C_x and T_{abs} . This overlap affects the trade-off between α_{sol} and ϵ_{th} for any SSC.

3.1.3. SSC model parameters

A STAC is often simply defined as SSC when it has a “high” solar absorptance α_{sol} and a “low” thermal emittance ϵ_{th} . A few scientific instruments, i.e. portable solar reflectometers and emissometers [131–134] allow a quick measurement of these FoMs in the field according to defined standards [87–89]. Due to their moderate spectral resolution, information is however lost about relevant spectral features of the STAC. The coating designer should thus rather rely on calibrated spectrophotometric data. As observed in Fig. 3 a, SSCs exhibit a rather smooth sigmoid shaped spectrum. This allows defining a spectral model $f_{SSC}(\lambda)$ for the SDHR, described by a few parameters that can be easily interpreted as specific FoMs for SSC, assuming the residual error is negligible.

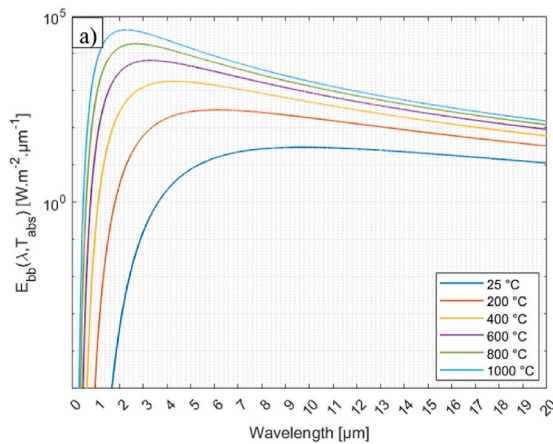
Simple models have been proposed in the literature, such as step functions and logistic functions [94,95]. The Heaviside unit step function has been expressed in (Eq. (4)), a modified step function [94] is described in (Eq. (11)), while a versatile logistic model [95] is

Table 3
Inventory of selected STAC opto-thermal FoMs.

Level	Label	FoM	Units	Variables	Target	Range
1	Solar absorptance	α_{sol}	[%]	SDHR, AM	Max	0–100%
	Thermal emittance	$\varepsilon_{th,calc}$	[%]	SDHR, T_{abs}	Min	0–100%
	SSC model	$f_{SSC}(\lambda)$	[–]	f_{shape} , $\lambda_{cut-off}$, asymptotes	Curve fit	0 ... 1
2	Selectivity ratio	Si	[–]	α_{sol} ; $\varepsilon_{th,calc}$; AM; T_{abs}	Max	>0
	Normalized selectivity ratio	Si^*	[–]	α_{sol} ; $\varepsilon_{th,calc}$; AM; T_{abs}	Max	Infinite
	Useful heat flux	\dot{q}_{use}''	[W/m ²]	α_{sol} ; $\varepsilon_{th,calc}$; C_{x} ; AM; h_{conv} ; T_{abs} ; T_{sky} ; T_{amb}	Max	>0
	Opto-thermal efficiency	η_{opt-th}	[%]	α_{sol} ; $\varepsilon_{th,calc}$; C_{x} ; AM; h_{conv} ; T_{abs} ; T_{sky} ; T_{amb}	Max	0–100%
	Trade-off factor	$Z_{trade-off}$	[–]	α_{sol} ; $\varepsilon_{th,calc}$; C_{x} ; AM; h_{conv} ; T_{abs} ; T_{sky} ; T_{amb}	[–]	Infinite
3	Max. Steady-State Temperature	$T_{SST,max}$	[K]	$\dot{q}_{use}'' = 0$	Max	>0
	Solar Reflective Index	SRI	[–]	$T_{SST,max}$, $T_{SST,white}$; $T_{SST,black}$	Min	–
	Normalized SRI	SRI^*	[%]	$T_{SST,max}$, $T_{ref,min}$; $T_{ref,max}$	Min	0–100%
	Thermal efficiency	$\eta_{thermal}$	[%]	$\eta_{coating,opt-th}$; η_{carnot}	Max	0–100%
	Peak efficiency temperature	$T_{peak,opt}$	[K]	$\eta_{thermal}$	Max	>0

formulated in (Eq. (12)). SSC spectral models are summarized in Table 4 with their characteristics. These models capture at least one of the following features:

- Cut-off wavelength $\lambda_{cut-off}$
- Shape factor f_{shape} , describing the steepness of the curve
- Asymptotical values, i.e. when $\lambda \rightarrow 0$ and $\lambda \rightarrow +\infty$



$$\rho_{SDHR}(\lambda) = \begin{cases} \rho_{low}; & \lambda \leq \lambda_{cut-off} \\ \rho_{high}; & \lambda > \lambda_{cut-off} \end{cases} \quad (11)$$

$$\rho_{SDHR}(\lambda) = \frac{L}{1 + \exp\left[f_{shape}\left(\frac{1}{\lambda} - \frac{1}{\lambda_{cut-off}}\right)\right]} + Offset \quad (12)$$

3.2. Level 2 FoMs

3.2.1. Selectivity indices

The next FoM is the selectivity ratio (Eq. (13)) [92,93], introducing here the symbol Si . This FoM allows a simple discrimination between SSCs and black coatings. The Si index is maximized for a SSC and close to 1 for a non-selective, grey body.

$$Si = \frac{\alpha_{sol}(AM)}{\varepsilon_{th}(T_{abs})} \quad (13)$$

One potential issue with this FoM occurs for SSC at low temperatures, because the thermal emittance could achieve infinitesimally small values. This would yield a nearly infinite Si value. As such, the Si index is re-normalized to correct this issue, coining the Simon's number Si^* as expressed in (Eq. (14)). With this variant formulation, a grey body achieves a null value and a SSC reaches a positive value.

$$Si^* = \ln(Si) \quad (14)$$

3.2.2. Useful heat flux

The useful heat flux \dot{q}_{use}'' (W·m⁻²) is a common FoM [96,97], already introduced in (Eq. (1)). This equation is further developed in (Eq. (15)) for the special case of a small flat or convex surface, e.g. a receiver tube, surrounded by an enclosure (view factor $F_{view} = 1$) at a temperature T_{sky} [135,136].

$$\dot{q}_{use}'' = \alpha_{sol}\dot{q}_{sol}'' - \varepsilon_{th}(T_{abs})\sigma(T_{abs}^4 - T_{sky}^4) - h_{conv}(T_{abs} - T_{amb}) \quad (15)$$

where h_{conv} is the convection heat transfer coefficient (Units: W/(m²·K)).

An analogous heat transfer coefficient h_{rad} can be defined for radiation (Eq. (16)):

$$h_{rad} = \frac{\varepsilon_{th}(T_{abs})\sigma(T_{abs}^4 - T_{sky}^4)}{T_{abs} - T_{sky}} \quad (16)$$

A dimensionless number Cr can be introduced to compare respective heat transfer coefficients for convection and radiation (Eq. (17)):

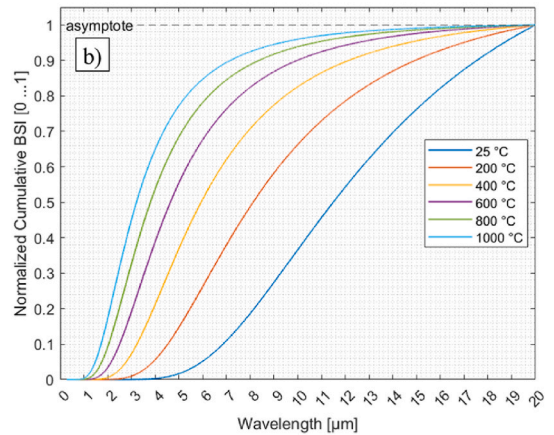


Fig. 7. Blackbody spectral irradiance. a) Planck's law of blackbody radiation for an absorber temperature ranging from 25 to 1000 °C b) Cumulative fraction of Stefan-Boltzmann law ($\sigma \cdot T^4$).

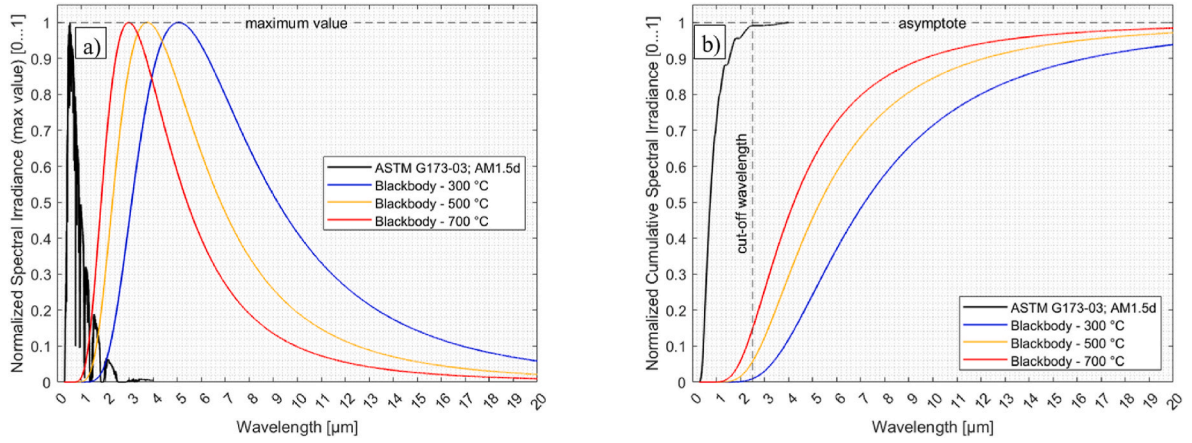


Fig. 8. Comparison of solar and blackbody spectral irradiances. a) Spectral irradiances normalized by their maximum value. b) Normalized cumulative spectral irradiances. The solar spectral irradiance is normalized by the integral value computed at AM1.5 (direct + circumsolar) from 0.28 to 4 μm , while the blackbody spectral irradiance is normalized with respect to Stefan Boltzmann law ($\sigma \cdot T^4$).

Table 4

Summary of SSC model parameterization.

Model	Unit step function	Ref. [94] 3 parameters	Ref. [95] 2 parameters	Ref. [95] 4 parameters	Logistic function (3 parameters)
Equation	(11)	(11)	(12)	(12)	(12)
Parameters and values	$\rho_{\text{low}} = 0$ $\rho_{\text{high}} = 1$ $\lambda_{\text{cut-off}} > 0$ $f_{\text{shape}} = +\infty$	$0 < \rho_{\text{low}} < 1$ $0 < \rho_{\text{high}} < 1$ $\lambda_{\text{cut-off}} > 0$ $f_{\text{shape}} = +\infty$	$L = 1$ Offset = 0 $\lambda_{\text{cut-off}} > 0$ $f_{\text{shape}} > 0$	$0 < L$ Offset > 0 $\lambda_{\text{cut-off}} > 0$ $f_{\text{shape}} > 0$	$0 < L$ Offset = 0 $\lambda_{\text{cut-off}} > 0$ $f_{\text{shape}} > 0$
# parameters	1	3	2	4	3
$\lambda_{\text{cut-off}}$	Explicit	Explicit	Explicit	Explicit	Explicit
f_{shape}	Not defined	Not defined	Explicit	Explicit	Explicit
Value at $\lambda_{\text{cut-off}}$	0	ρ_{low}	$L/2 = 0.5$	Offset + $L/2$	$L/2$
Asymptote 1 $\lambda \rightarrow 0$	0	ρ_{low}	Offset = 0	Offset	Offset = 0
Asymptote 2 $\lambda \rightarrow +\infty$	1	ρ_{high}	$\frac{L}{1 + \exp\left[f_{\text{shape}}\left(-\frac{1}{\lambda_{\text{cut-off}}}\right)\right]} + \text{Offset}$		

$$Cr = \ln\left(\frac{h_{\text{conv}}}{h_{\text{rad}}}\right) \quad (17)$$

The Cr number approaches zero if convection and radiation are of the same order of magnitude. It is expressed in logarithmic form as both h_{conv} and h_{rad} coefficients can be infinitesimally small, respectively for a

(Eq. (18)) can also be formulated in integral form (Eq. (20)), if spectral data is available over a given spectral range $[\lambda_1 \dots \lambda_3]$, assuming further that T_{sky} is negligible in comparison to T_{abs} :

$$\dot{q}_{\text{use}}'' \approx C_x \int_{\lambda_1}^{\lambda_2} [1 - \rho_{\text{SDHR}}(\lambda, \theta, T_{\text{amb}})] G_{\text{sol}}(\lambda, AM) d\lambda - \int_{\lambda_1}^{\lambda_3} [1 - \rho_{\text{SDHR}}(\lambda, \theta, T_{\text{amb}})] E_{\text{bb}}(\lambda, T_{\text{abs}}) d\lambda \quad (20)$$

vacuum enclosure and a low emittance coating. According to our assumptions (Section 2.2), our analysis is carried out for a regime where convection is negligible in comparison to radiation heat transfer (i.e. $Cr \rightarrow -\infty$).

Neglecting convection (Eq. (16)), simplifies to (Eq. (18)) in lumped form:

$$\dot{q}_{\text{use}}'' = \alpha_{\text{sol}} \dot{q}_{\text{sol}}'' - \varepsilon_{\text{th}}(T_{\text{abs}}) \sigma (T_{\text{abs}}^4 - T_{\text{sky}}^4) \quad (18)$$

Where \dot{q}_{sol}'' is defined according to the following integral (Eq. (19)):

$$\dot{q}_{\text{sol}}'' = C_x \int_{\lambda_1}^{\lambda_2} G_{\text{sol}}(\lambda, AM) d\lambda \quad (19)$$

For a STAC performance comparison, the absolute value \dot{q}_{use}'' in W/m^2 may be difficult to interpret out of context, the marginal useful heat difference $\Delta \dot{q}_{\text{use}}''$ is thus considered to compare for instance the performance of a black coating and a SSC at a given operation point $\{C_x; T_{\text{abs}}\}$ (Eq. (21)):

$$\Delta \dot{q}_{\text{use}}''(C_x, T_{\text{abs}}) = \dot{q}_{\text{use,black}}'' - \dot{q}_{\text{use,SSC}}'' \quad (21)$$

For a given operation point $\{C_x; T_{\text{abs}}\}$, the marginal useful heat difference is here defined positive if the black coating performs better than a SSC, and negative otherwise.

3.2.3. Opto-thermal efficiency

The coating opto-thermal efficiency η_{opt-th} is a FoM [11–13,30,38,39] defined as the ratio of the useful heat flux \dot{q}_{use}'' and the concentrated solar flux \dot{q}_{sol}'' . Assuming negligible convection ($Cr \rightarrow -\infty$), η_{opt-th} can be expressed in lumped form (Eq. (22)):

$$\eta_{opt-th} = \frac{\dot{q}_{use}''}{\dot{q}_{sol}''} \approx \alpha_{sol} - \frac{\varepsilon_{th}(T_{abs})\sigma(T_{abs}^4 - T_{sky}^4)}{\dot{q}_{sol}''} \quad (22)$$

This FoM can also be written in integral form (Eq. (23)), by dividing (Eq. (20)) and (Eq. (19)):

$$\eta_{opt-th} \approx \frac{C_x \int_{\lambda_1}^{\lambda_2} [1 - \rho_{SDHR}(\lambda, \theta, T_{amb})] G_{sol}(\lambda, AM) d\lambda - \int_{\lambda_1}^{\lambda_2} [1 - \rho_{SDHR}(\lambda, \theta, T_{amb})] E_{bb}(\lambda, T_{abs}) d\lambda}{C_x \int_{\lambda_1}^{\lambda_2} G_{sol}(\lambda, AM) d\lambda} \quad (23)$$

The marginal opto-thermal efficiency difference $\Delta\eta_{opt-th}$ is expressed in (Eq. (24)) as above in (Eq. (21)) to compare a black coating and a SSC at a given operation point $\{C_x, T_{abs}\}$:

$$\Delta\eta_{opt-th}(C_x, T_{abs}) = \eta_{opt-th, black} - \eta_{opt-th, SSC} \quad (24)$$

3.2.4. Trade-off factor

The coating opto-thermal efficiency η_{opt-th} allows deriving a first trade-off factor $Z_{trade-off}$ [30,98], a compound FoM describing the trade-off between α_{sol} and ε_{th} FoMs, as a function of the operation point $\{C_x, T_{abs}\}$. Partial derivatives are expressed in (Eq. (25)):

$$\frac{\partial\eta_{opt-th}}{\partial\alpha_{sol}} = 1; \quad \frac{\partial\eta_{opt-th}}{\partial\varepsilon_{th}} = - \frac{\sigma(T_{abs}^4 - T_{sky}^4)}{C_x \int_{\lambda_1}^{\lambda_2} G_{sol}(\lambda, AM) d\lambda} \quad (25)$$

The $Z_{trade-off}$ is defined in (Eq. (26)) by dividing both partial derivatives in (Eq. (25)):

$$Z_{trade-off} = \frac{\Delta\varepsilon_{th}}{\Delta\alpha_{sol}} = - \frac{C_x \int_{\lambda_1}^{\lambda_2} G_{sol}(\lambda, AM) d\lambda}{\sigma(T_{abs}^4 - T_{sky}^4)} \quad (26)$$

According to (Eq. (26)), varying α_{sol} by 1% point (p.p.) has the same effect on the opto-thermal efficiency η_{opt-th} as varying ε_{th} by $-Z_{trade-off}$ p.p. The solar absorptance α_{sol} is thus a dominant opto-thermal FoM. However, its initial value for a STAC should be above 95%, the

remaining useful range for improvement is thus limited. The influence of the thermal emittance ε_{th} depends on the operating point $\{C_x, T_{abs}\}$.

A similar sensitivity analysis as in (Eq. (25)) could be derived with respect to the parameter C_x , yielding further trade-off factors between the respective STAC and the concentrator designs. The η_{opt-th} FoM can be improved either by increasing solar absorptance α_{sol} , reducing thermal emittance ε_{th} or increasing concentration factor C_x , as illustrated in Table 5.

Paradoxically, a sensitivity analysis of η_{opt-th} with respect to the parameter T_{abs} yields a negative value, i.e. the STAC opto-thermal efficiency decreases at higher temperature. This does not reflect the influence of absorber temperature T_{abs} on the thermal efficiency $\eta_{thermal}$ of

the thermodynamic cycle.

3.3. Level 3 FoMs

3.3.1. Maximum steady-state temperature

The next FoM is the maximum Steady-State Temperature $T_{SST,max}$, also referred to as the “stagnation” temperature [92,99]. This parameter is measurable for a high temperature STAC in a non-destructive setup [93], for a low concentration factor ($C_x < 10$), otherwise the STAC may exceed its maximal operating temperature and would suffer an irreversible degradation.

By definition, $T_{SST,max}$ corresponds to the temperature of the STAC when no useful heat can be extracted from the absorber, i.e. (Eq. (15)) equals zero. All the absorbed solar flux is then radiated away by the STAC. Neglecting convection losses (Eq. (18)), can be rewritten as in (Eq. (27)).

$$T_{SST,max} \approx \left[\frac{\alpha_{sol}(AM)\dot{q}_{sol}'' + \varepsilon_{th}(T_{SST,max})\sigma T_{sky}^4}{\varepsilon_{th}(T_{SST,max})\sigma} \right]^{0.25} \quad (27)$$

The parameter $T_{SST,max}$ appears on both sides of the equations, as ε_{th} is temperature dependent for reference materials (Eq. (27)). is hence solved numerically for $T_{SST,max}$.

3.3.2. Solar reflectance indices

The solar reflective index SRI [87–89,100,101] is another standard FoM, rather used in the building industry to characterize construction materials suitable for mitigating the Urban Heat Island (UHI) phenomenon [137–141]. This FoM is calculated on the basis of α_{sol} and ε_{th} values measured with portable devices [87–89,131–134]. Its original formulation is related to the computation of maximum steady-state temperature $T_{SST,max}$, outlined in the previous subsection.

For building applications (Eq. (15)), is solved for $T_{SST,max}$ with the following standard parameters [100]:

- $\dot{q}_{sol}'' = 1000 \text{ W m}^{-2}$ ($C_x = 1$; AM1.5; global radiation [124]);
- $h_{conv} = 12 \text{ W m}^{-2} \text{ K}^{-1}$
- $T_{sky} = 300 \text{ K}$; $T_{amb} = 310 \text{ K}$

The $T_{SST,max}$ value computed for a given material is then compared to two reference bodies, for which stagnation temperatures are also computed as outlined above:

- Reference black surface: ($\alpha_{sol} = 0.95$; $\varepsilon_{th} = 0.90$)
o Temperature $T_{black, SST}$ (82.6 °C)

Table 5

Sensitivity of opto-thermal efficiency η_{opt-th} ; G_{sol} (AM1.5 d) = 900 W/m²; $T_{abs} = 600$ °C, $T_{sky} = 25$ °C.

Scenario	α_{sol} [0 ... 1]	ε_{th} [0 ... 1]	C_x [–]	η_{opt-th} [%]
Ref A (SSC, PTC)	0.95	0.15	100	89.6%
Increase α_{sol} (↑)	0.96 (+ 1 p.p.)	0.15	100	90.6% (+ 1 p.p.)
Decrease ε_{th} (↓)	0.95	0.122 (-2.8 p.p.)	100	90.6% (+ 1 p.p.)
Increase C_x (↑)	0.95	0.15	123 (+ 23%)	90.6% (+ 1 p.p.)
Ref B (Black, CRS)	0.95	0.90	1000	91.7%
Increase α_{sol} (↑)	0.96 (+ 1 p.p.)	0.90	1000	92.7% (+ 1 p.p.)
Decrease ε_{th} (↓)	0.95	0.65 (-30 p.p.)	1000	92.7% (+ 1 p.p.)
Increase C_x (↑)	0.95	0.90	1400 (+ 40%)	92.7% (+ 1 p.p.)

- Reference white surface; ($\alpha_{sol} = 0.20$; $\varepsilon_{th} = 0.90$)
- o Temperature $T_{white, SST}$ (44.7 °C)

The SRI is computed according to (Eq. (28)):

$$SRI = 100 \frac{T_{black, SST} - T_{SST, max}}{T_{black, SST} - T_{white, SST}} \quad (28)$$

A low SRI value indicates a cool roof material, while a high SRI values indicates a hot roof material. A few issues have been expressed for this FoM in the building industry [101]. Although the SRI is expressed in percent, its value can reach either negative values or values above 100, as the reference black and white materials are not optimized: the solar reflectance or “*albedo*” index is varying between 0.2 and 0.95, while the thermal emittance or “*melano*” index is constant at 0.9.

The SRI calculation is adapted in this paper, first by setting adapted boundary conditions relevant for concentrated solar power, according to the modelling assumptions (Section 2.2):

- Solar irradiance: AM1.5; direct + circumsolar [124].
- Variable concentration factor C_x variable
- Negligible convection losses ($h_{conv} = 0$)
- Sky temperature $T_{sky} = 25$ °C

Furthermore, a renormalized SRI* FoM is defined (Eq. (29)), introducing spectral selective reference coatings, which spectral profiles are defined according to (Eq. (11)) [94]:

- Reference “cold” coating:
 - o $\{\lambda_{cut-off} = 2.5 \mu m; \rho_{low} = 0.99; \rho_{high} = 0.01\}$
- Reference “hot” coating:
 - o $\{\lambda_{cut-off} = 2.5 \mu m; \rho_{low} = 0.01; \rho_{high} = 0.99\}$

$$SRI^* = 100 \frac{T_{hot, ref} - T_{SST, max}}{T_{hot, ref} - T_{cold, ref}} \quad (29)$$

The choice is made to define two reference coatings with symmetrical spectral selectivity (S_i, S_i^*), i.e. one “cold” reference coating (low α_{sol} , high ε_{th}) and one “hot” reference coating (high α_{sol} , low ε_{th}). The “hot” reference coating is nearly equivalent to the ideal SSC introduced in Section 2.3, while the “cold” reference coating acts as an “anti-solar” surface [142]. Instead of defining a constant value for α_{sol} and ε_{th} , spectral profiles are defined to achieve a constant α_{sol} value while achieving a realistic ε_{th} value at higher temperature.

3.3.3. Thermal efficiency and peak efficiency temperature

The last FoMs included in this review are the thermal efficiency $\eta_{thermal}$ [11,12,96,97] and the peak efficiency temperature $T_{peak, opt}$. The

thermal efficiency of a thermodynamic cycle is bounded by an upper limit, defined by the Carnot cycle (Eq. (30)):

$$\eta_{Carnot} = 1 - \frac{T_{sink, cold}}{T_{sink, hot}} \quad (30)$$

where $T_{sink, cold}$ and $T_{sink, hot}$ respectively correspond to the temperature of the cold and hot heat sinks. In practice, only a fraction $f_{Carnot} \sim 0.7$ [12] is accessible due to engineering limitations.

The thermal efficiency $\eta_{thermal}$ is thus formulated as a product in (Eq. (31)):

$$\eta_{thermal} = \eta_{opt-th} \cdot f_{Carnot} \cdot \eta_{Carnot} \quad (31)$$

Assuming negligible convection ($Cr \rightarrow \infty$), a cold heat sink $T_{sink, cold}$ with a sky temperature T_{sky} , a hot heat sink $T_{sink, hot}$ with absorber temperature T_{abs} and assuming a fraction $f_{Carnot} = 0.70$ (Eq. (32)), is derived:

$$\eta_{Carnot} \approx f_{Carnot} \left(\alpha_{sol} - \frac{\varepsilon_{th}(T_{abs}) \sigma (T_{abs}^4 - T_{sky}^4)}{\dot{q}_{sol}''} \right) \cdot \left(1 - \frac{T_{sky}}{T_{abs}} \right) \quad (32)$$

The thermal efficiency $\eta_{thermal}$ equals zero for two temperatures, i.e. sky temperature and maximal stagnation temperature. It peaks at an optimal absorber surface temperature $T_{peak, opt}$ (Eq. (33)).

$$\left. \frac{\partial \eta_{Carnot}}{\partial T_{abs}} \right|_{T_{peak, opt}} = 0 \quad (33)$$

4. Results and discussion

4.1. Level 1 FoMs

4.1.1. Solar absorptance

The solar absorptance α_{sol} is calculated according to (Eq. (6)) for different AM values, ranging from AM0 to AM5. Results are illustrated in Fig. 9 a. for reference coatings (Fig. 3), while the cumulative solar absorptance (Eq. (7)) is shown in Fig. 9 b for AM1.5 (direct + circumsolar).

In Fig. 9 a, ideal SSC and blackbody coatings both achieve a maximum α_{sol} value (100%), as these coatings absorb all the solar radiation. The reference SSC reaches a α_{sol} value of 94.6% (AM1.5), while the α_{sol} value reaches 96.6% (+2 p. p.) for the reference black coating. This coating reaches an α_{sol} value above 96% and is thus qualified as HSA.

As can be observed in Fig. 9 a, the AM variable has a weak influence on the α_{sol} value. For the reference black coating, the same α_{sol} value (96.6%) is computed from AM0 to AM3, meanwhile the α_{sol} value varies

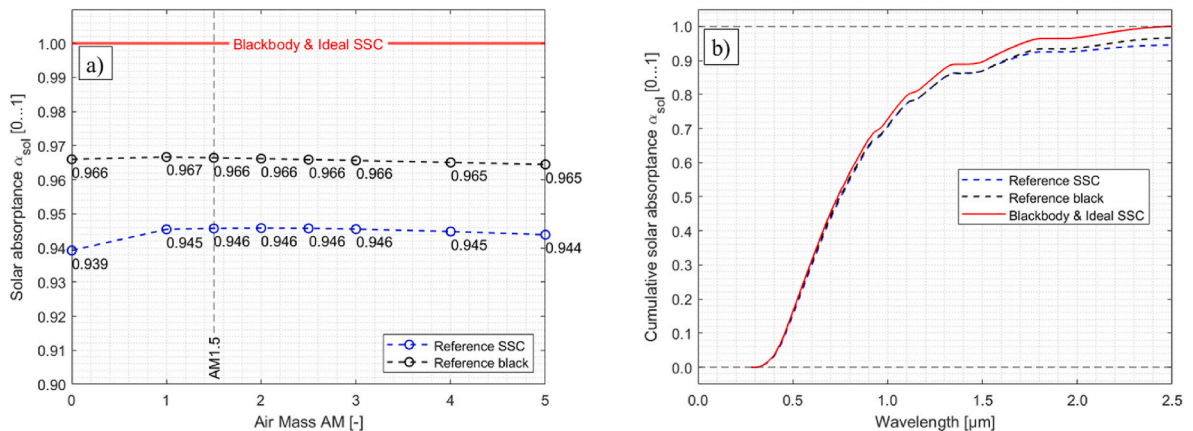


Fig. 9. Calculation of α_{sol} (Eq. (6)) from 0.28 to 2.5 μm a) as a function of AM for reference coatings. b) Cumulative solar absorptance according to (Eq. (7)) considering the coating SDHR.

from 93.9% (AM0) to 94.6% (AM1.5 ... 3) for the reference SSC.

Looking at the cumulative solar absorptance for AM1.5 (Fig. 9b), one observes that the 2 p. p. difference at between the reference black coating and SSC first appears and amplifies around 1.7 μm , in the shortwave IR range. At this same wavelength, the reference black coating is already 2.7 p. p. from the ideal profile (red curve) to achieve a maximal α_{sol} value. This diagram offers a finer appreciation of the spectral deviations to compare and improve STAC formulations.

Maximal solar absorptance ($\sim 100\%$) has been achieved so far with Carbon Nanotubes (CNT) [143]. Such “space black” coatings are typically applied by vacuum deposition or spraying processes. These high-performance coatings are rather designed for stray light suppression on sensitive optical devices for space missions [144,145], considering their cost of application, high temperature stability and environmental durability [146]. For high temperature STAC, the upper α_{sol} limit for stable formulations reaches 98% [98]. A Haynes 230 metal substrate oxidized at temperatures above 700 $^{\circ}\text{C}$ reaches a α_{sol} value above between 92 and 94% [31,98], due to the formation of a duplex oxide scale [147]. For CRS applications, a re-coating threshold value of 95% is reported [37]. The useful α_{sol} range for high temperature STAC is thus restricted from 90 to 100%. An increase of a few tenth of a p. p. represents a significant improvement for the solar absorptance.

4.1.2. Thermal emittance

The thermal emittance ϵ_{th} is computed according to (Eqs. (8) and (9)) for an absorber temperature T_{abs} ranging from 25 to 1000 $^{\circ}\text{C}$ for the reference coatings and shown in Fig. 10 a. The cumulative thermal emittance is plotted in Fig. 10 b. for $T_{\text{abs}} = 600$ $^{\circ}\text{C}$. It is worth remembering that the coverage fraction of Stefan Boltzmann law increases with temperature (Fig. 7b) and the spectral calculation is here performed over the spectral range [0.28 ... 20 μm] for the available spectral data (Fig. 3a).

ISO 22975-3 [83] recommends for instance a spectral range from 2 to 50 μm for lower temperatures, extrapolating spectral data beyond 20 μm . Omitting data above 20 μm would influence the ϵ_{th} calculation. For the reference black coating, its spectral reflectance should remain low (Fig. 3a) and the ϵ_{th} value should thus increase moderately by a few percent points. For a SSC, the spectral reflectance reaches an asymptotical value in the IR range (Fig. 3a) and the extrapolation can be justified, the ϵ_{th} value should decrease marginally by a few percent points.

From 25 to 1000 $^{\circ}\text{C}$, the ideal SSC reaches the lowest ϵ_{th} value for any temperature (Fig. 10a). Its ϵ_{th} value is lower than 10% below and 600 $^{\circ}\text{C}$. For the reference SSC, the ϵ_{th} value approaches 23% at 600 $^{\circ}\text{C}$. For the reference black coating, the ϵ_{th} value reaches 78% at 600 $^{\circ}\text{C}$. The ideal blackbody is obviously the worst coating, with a maximal thermal

emittance (100%).

The useful optimization range for the ϵ_{th} FoM is constrained, although the ideal SSC is here only optimized to maximize α_{sol} . This value is 55 p. p. above the reference SSC and 68 p. p. above the ideal SSC at the same temperature. The ϵ_{th} value can thus be potentially improved by a few decades in the best case. The temperature dependence of the ϵ_{th} value is more pronounced for SSCs than for black coatings. For SSCs, the ϵ_{th} value increases at higher temperature. For a black coating, this temperature dependence is moderate.

Looking at the cumulative thermal emittance (Fig. 10b) calculated at 600 $^{\circ}\text{C}$, one can notice that asymptote ϵ_{th} value is reached earlier on for SSCs. In the case of the ideal SSC; there is a sharp transition at 2.5 μm (cut-off wavelength). Before this wavelength, the ideal SSC is first aligned with the ideal blackbody. Beyond 2.5 μm , the ideal SSC does not emit radiation. The reference SSC converges to 99% of its asymptote ϵ_{th} value around 12 μm . For black coatings, the asymptotical convergence is not completed yet at 20 μm , this is even more pronounced at lower temperatures.

Instead of reporting ϵ_{th} values at arbitrary temperature levels, temperature correlations or tables should be documented, for example with fourth order polynomial fits. Such polynomial fits are implemented for further calculations in this paper.

4.1.3. SSC model parameters

SSC models (Table 4) are fitted to the reference SSC (Fig. 3a), applying ordinary least squares for logistic models (Eq. (12)) to minimize the root mean square error (RMSE). Fitted parameter values are listed in Table 6. Spectral curves are shown in Fig. 11 a, while residuals are shown for logistic functions in Fig. 11 b.

A better fit is achieved for the reference SSC (Fig. 11a) with logistic models (Eq. (12)) than with step functions (Eq. (11)). The residual analysis (Fig. 11b) indicates that the maximal deviation is observed in the shortwave range (< 2.5 μm), which would directly affect the α_{sol} calculation (Eq. (6)). A higher noise is observed beyond 2.5 μm for FTIR data. A spike is observed at 4.3 μm , corresponding to a strong CO_2 absorption band, as the instrument has not been purged during the measurement.

The identified parameters of the SSC spectral curve slightly differ from one logistic model to the other, depending on the applied constraints for (Eq. (12)). The cut-off wavelength $\lambda_{\text{cut-off}}$ spans from 2.4 to 2.46 μm , while the spectral shape factor f_{shape} spans from 7.37 to 7.92. The logistic model with 4 parameters seems to be the most flexible and accurate model, with the minimal RMSE value.

These logistic models can simulate the ideal blackbody and SSC for asymptotical parameter values:

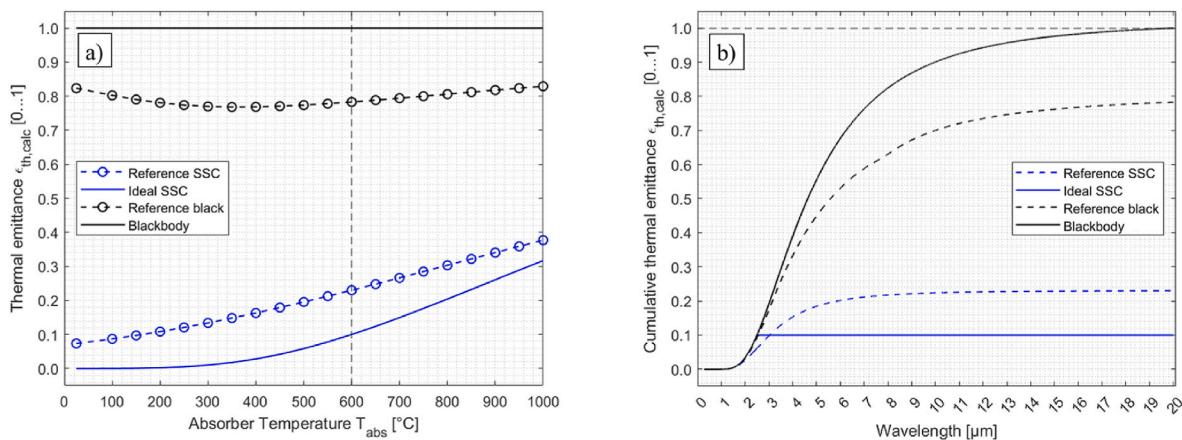
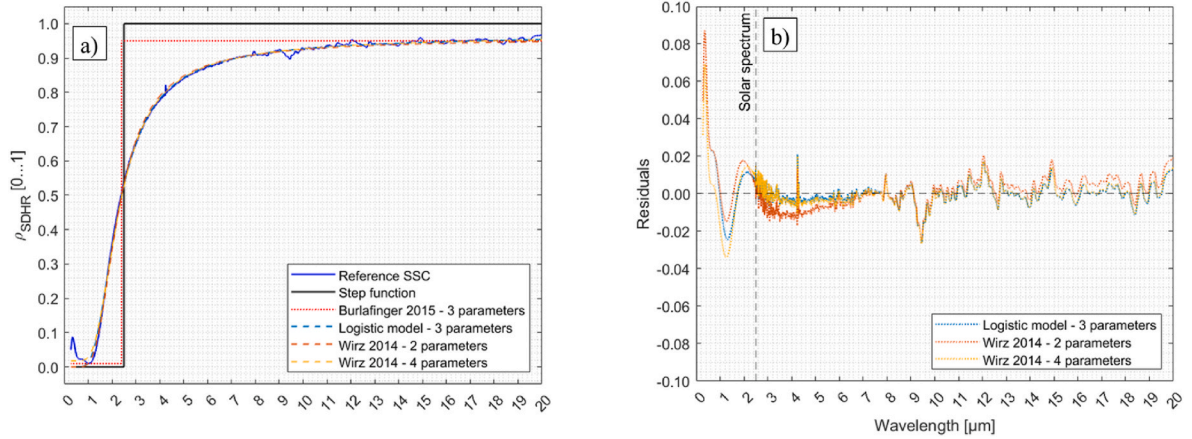
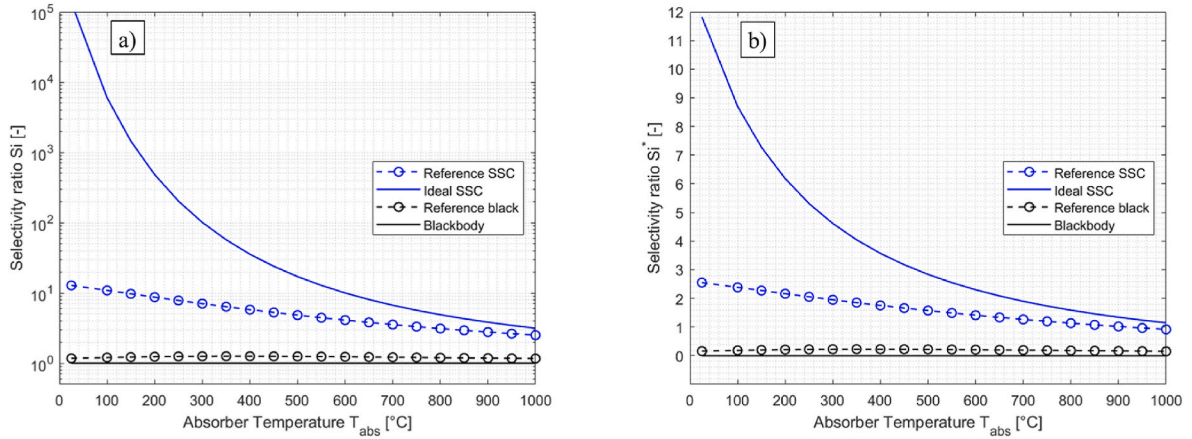


Fig. 10. Calculation of thermal emittance ϵ_{th} (Eqs. 8-9) a) as a function of T_{abs} for reference coatings. b) Cumulative thermal emittance at 600 $^{\circ}\text{C}$ according to (Eq. (10)) considering the coating SDHR.

Table 6

Results of SSC spectral model curve fitting applying ordinary least squares.

Model	Ref. [94] (3 parameters)	Ref. [95] (2 parameters)	Ref. [95] (4 parameters)	Logistic function (3 parameters)
Identified parameters	$\rho_{low} = 0.01$ $\rho_{high} = 0.95$ $\lambda_{cut-off} = 2.4 \mu m$	$L = 1$ Offset = 0 $\lambda_{cut-off} = 2.4003 \mu m$ $f_{shape} = 7.9179$	$L = 0.9970$ Offset = 0.0182 $\lambda_{cut-off} = 2.4645 \mu m$ $f_{shape} = 7.6227$	$L = 1.0207$ Offset = 0 $\lambda_{cut-off} = 2.4367 \mu m$ $f_{shape} = 7.3696$
RMSE	0.1182	0.0112	0.0093	0.0101

**Fig. 11.** Spectral curve fitting of reference SSC with parameterized spectral models (Table 4). a) Comparison of spectral models. b) Residuals for logistic models derived from (Eq. (12)).**Fig. 12.** Selectivity indices as a function of absorber temperature T_{abs} a) Selectivity ratio Si b) normalized selectivity ratio Si^* .

- blackbody: {Offset = 0; $L \rightarrow 0$; $\lambda_{cut-off} \rightarrow +\infty$; $f_{shape} \rightarrow +\infty$ }
- ideal SSC: {Offset = 0; $L \rightarrow 1$; $\lambda_{cut-off} \rightarrow 2.5 \mu m$; $f_{shape} \rightarrow +\infty$ }

However, logistic functions are not appropriate to model accurately the black coating spectrum.

4.2. Level 2 FoMs

4.2.1. Selectivity indices

Selectivity indices Si and Si^* (Eq. (13) and (14)) are plotted for reference coatings at AM1.5 as a function of T_{abs} in Fig. 12. The Si index spans a wide range, from 1 for an ideal blackbody to $\sim 10^4$ for an ideal SSC at $100^{\circ}C$. After logarithmic scaling, the Si^* index spans from 0 for an ideal blackbody to ~ 10 for an ideal SSC at $100^{\circ}C$. As an order of magnitude, the best Si^* value that can be achieved at $600^{\circ}C$ is about 2.3 for an ideal SSC, i.e. the ϵ_{th} value can only be reduced down up to a tenth of α_{sol} for a STAC, as the contribution of blackbody spectral irradiance below $2.5 \mu m$ increases at higher temperatures.

Selectivity indices Si and Si^* are temperature dependent, because of the temperature dependence of the ϵ_{th} FoM, especially for selective coatings. The selectivity of a SSC thus decreases at a higher absorber temperature, as the ϵ_{th} value increase.

4.2.2. Useful heat flux and opto-thermal efficiency

Marginal differences in useful heat flux $\Delta q_{use}''$ (Eq. (21)) and opto-thermal efficiency $\Delta \eta_{opt-th}$ (Eq. (24)) between the black coating and the reference SSC are plotted in Fig. 13 as a contour map of two variables: the concentration factor C_x and the absorber surface temperature T_{abs} .

The α_{sol} value for reference black coating is 2 p. p. higher 2 p. p. higher than in comparison to the α_{sol} value for the reference SSC (Section 4.1.1). This advantage outweighs the benefit of a low ϵ_{th} value for high C_x and low T_{abs} values (Fig. 13, bottom right corners). In these regions, i. e. $\Delta q_{use}''$ and $\Delta \eta_{opt-th}$ are both positive and the black coating is more efficient than the reference SSC. The reference SSC is more efficient in

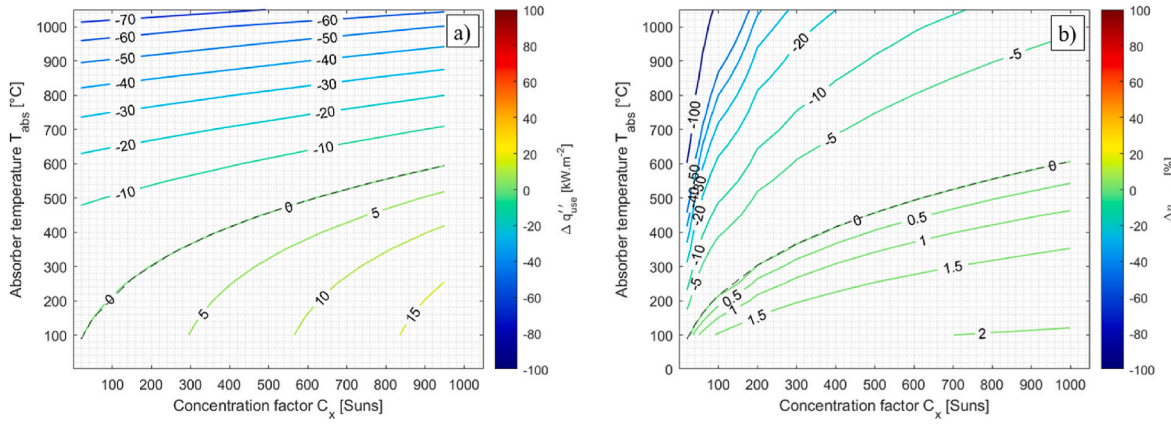


Fig. 13. Comparison of the reference black coating and SSC as a function of C_x and T_{abs} . a) Marginal useful heat flux difference $\Delta q''_{use}$ b) Marginal opto-thermal efficiency $\Delta \eta_{opt-th}$.

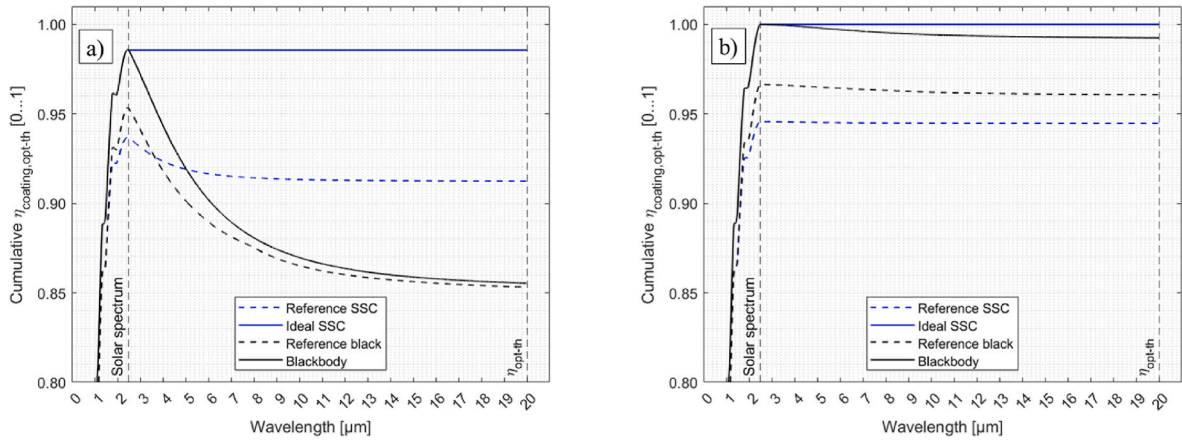


Fig. 14. Spectral analysis of STAC opto-thermal efficiency. a) $C_x = 250$, $T_{abs} = 600$ °C. b) $C_x = 850$, $T_{abs} = 300$ °C.

comparison to the black coating for low C_x and high T_{abs} values (Fig. 13, top left corners). A Pareto front can be identified on both contour maps (Fig. 13, black dotted line), where both coatings are equally efficient.

For PTC configurations, the C_x value is typically lower than 100 and the temperature ranges from 300 up to 600 °C. For this configuration, Fig. 13 confirms that a SSC is more efficient than a black coating. For a CRS configuration, the allowable flux density (AFD) [72–76] are implemented for a molten salt HTF to avoid metal corrosion. For the Solar Two power plant [26,27,72] A solar flux of 850 kW m^{-2} is allowed at the 290 °C receiver inlet, while a lower solar flux of 240 kW m^{-2} is allowed at the 565 °C receiver outlet. Such constraints are rather favorable for the black coating according to Fig. 13, although the Pareto front is crossed. The real SSC is thus not always optimal for this later application. In order to select the most efficient coating, the $\Delta q''_{use}$ or $\Delta \eta_{opt-th}$ FoMs have to be integrated over the relevant C_x and T_{abs} domains, considering their correlation.

4.2.3. Comparison of spectral STAC opto-thermal efficiencies

Respective STAC cumulative opto-thermal efficiencies are analyzed spectrally according to (Eq. (20); $\lambda_2 = 2.5 \text{ μm}$; $\lambda_3 = 20 \text{ μm}$) in Fig. 14. Two extreme configurations are selected according to the above discussion, i.e. one configuration in favor of the reference SSC (Fig. 14 a; $C_x \sim 250$ suns, $T_{abs} \sim 600$ °C) and another in favor of the reference black coating (Fig. 14 b; $C_x \sim 850$ suns, $T_{abs} 300$ °C). These graphs illustrate a “spectral race”, i.e. the detailed integration from 0.28 μm up to a wavelength λ .

It is worth remarking from Fig. 14 that The STAC ranking differ

slightly from one configuration to the other. In both cases, the ideal SSC is best ranked STAC (blue line). All other curves peak around 2.5 μm , at which point solar radiation is fully absorbed.

In the first case (Fig. 14 a; $C_x = 250$, $T_{abs} = 600$ °C), the reference SSC ranks second (blue dotted line), the ideal blackbody third (black line) and the reference black coating fourth (black dotted line), nearly on par with the ideal blackbody. The gap in η_{opt-th} between the reference SSC

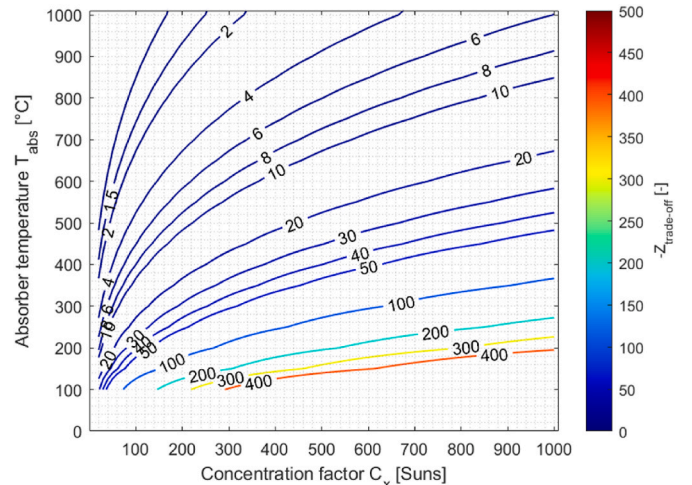


Fig. 15. Contour map of trade-off factor as a function of C_x and T_{abs} .

and the ideal blackbody after integration up to $20\ \mu\text{m}$ is about 6 p. p. The curve for the reference SSC respectively crosses the reference black coating curve at $3.5\ \mu\text{m}$ and the ideal BB at $5\ \mu\text{m}$.

In the second case (Fig. 14 b; $C_x = 850$, $T_{\text{abs}} = 300\ ^\circ\text{C}$), the ranking is different: the ideal blackbody ranks second (black line), the reference black coating third (black dotted line) and the reference SSC fourth (blue dotted line). This time, the spectral curves do not cross. The reference SSC is the least efficient coating this time.

Both graphs offer a valuable perspective on the respective benefits of SSC and black coatings in terms of opto-thermal efficiency. In the first case, improving the coating spectral selectivity is relevant. In the second case, maximizing α_{sol} is more relevant. Improving the coating spectral selectivity becomes a secondary goal.

4.2.4. Trade-off factor

The trade-off factor $Z_{\text{trade-off}}$ (Eq. (26)) is plotted as a function of C_x and T_{abs} in Fig. 15. This figure confirms previous observations made in Sections 4.2.2 and 4.2.3. At ($C_x \sim 250$ suns, $T_{\text{abs}} \sim 600\ ^\circ\text{C}$), $Z_{\text{trade-off}} \sim -6.85$, i.e. an increase of 1 p. p. in α_{sol} has the same effect on $\eta_{\text{opt-th}}$ as reducing ϵ_{th} by 6.85 p. p. At ($C_x \sim 850$ suns, $T_{\text{abs}} 300\ ^\circ\text{C}$), $Z_{\text{trade-off}} \sim 134$, i.e. an increase of 1 p. p. in α_{sol} would be compensated by a reduction of -134 p. p. in ϵ_{th} . Considering the respective useful optimization ranges discussed in sections 3.1.1. and 3.1.2, it is confirmed that selecting a SSC is not necessarily the best option, the operating range $\{C_x; T_{\text{abs}}\}$ has to be carefully examined.

4.3. Level 3 FoMs

4.3.1. Maximum steady-state temperature

The maximum Steady-State Temperature $T_{\text{SST,max}}$ is calculated for reference STAC (Section 2.3) and further references introduced in Section 3.3.2. according to (Eq. (27)). The results are shown in Fig. 16 a on a semi-log plot while the search process is illustrated in Fig. 16 b at $C_x = 1000$ for reference STAC. The T_{abs} variable is swept beyond the allowed maximum operating temperature ($600\ ^\circ\text{C}$).

$T_{\text{SST,max}}$ increases with respect to C_x according to a logarithmic profile, in compliance with (Eq. (27)). According to thermodynamic constraints, $T_{\text{SST,max}}$ cannot exceed the apparent sun temperature ($T_{\text{sun}} = 5777\ \text{K}$) and the upper theoretical bound concentration factor C_x is limited to 215 for linear focusing concentrators and 46,250 for point focusing concentrators [96,97].

For the $T_{\text{SST,max}}$ FoM, the following STAC ranking is observed in Fig. 16 a: i) Ideal and reference SSC achieve the highest $T_{\text{SST,max}}$ value (blue line and blue dotted line), ii) The reference black coating ranks third (black dotted line) and the ideal blackbody ranks fourth (black

line).

More precisely, the ideal SSC ranks first up to $C_x = 750$. The reference SSC then surpasses the ideal SSC beyond $C_x = 750$, only by a few Kelvins. It is worth remarking that ϵ_{th} curves shown in Fig. 10 a actually cross for SSCs around $T_{\text{abs}} = 1400\ ^\circ\text{C}$, i.e. the ideal SSC has then a higher thermal emittance than the reference SSC. The ideal SSC is thus not optimized for high temperatures.

This reasoning is of course hypothetical, as the reference SSC is not designed to withstand such high temperature levels. In practice, it is technically impossible to measure $T_{\text{SST,max}}$ at high solar fluxes in a non-destructive setup, as irreversible degradation of the STAC and the metal substrate is expected.

4.3.2. Solar reflectance indices

Solar reflectance indices SRI and SRI* are respectively calculated according to (Eq. (28)) and (Eq. (29)) for all reference coatings defined in this paper. The results are plotted for SRI in Fig. 17 a and for SRI* in Fig. 17 b, as a function of C_x .

In Fig. 17, The SRI scaling bias is confirmed, as several reference coatings achieve a value beyond the interval $[0-100]$. For instance, All STAC except the ideal blackbody reach negative SRI values. This is explained according to Fig. 16 a, these STAC reach a higher stagnation temperature $T_{\text{SST,max}}$ in comparison to the SRI black reference. The SRI scale is also not adapted for the cold reference introduced to define the SRI* FoM, as this coating achieves a SRI approaching 200!

The normalized SRI* FoM is bound between 0 and 100% for all defined reference coatings (Fig. 17b), except for the ideal SSC, which SRI* value is negative, but not exceeding -1 . SRI* decreases with increasing C_x and the hierarchy observed for $T_{\text{SST,max}}$ is respected (Fig. 16 a.). All STAC achieve a SRI* lower than 50%. The SRI white reference reaches the highest SRI* value ($>50\%$).

A correlation can be noticed between selectivity indices (Si/Si^*) and $T_{\text{SST,max}}$, justifying a rescaling of the SRI FoM. This is illustrated in Fig. 18, taking respectively as x-axis and y-axis the thermal emittance ϵ_{th} and the solar absorptance α_{sol} .

In Fig. 18 a, the diagram can be divided into two sectors along the axis $\text{Si}^* = 0$ (grey body, black dotted line). Reference STAC are located in the upper half (blue and black lines). SRI reference coatings span on a vertical red dotted line, as their ϵ_{th} is constant (90%). SRI* references span on an orthogonal line to the axis $\text{Si}^* = 0$ (purple dotted line). As Si^* increases, the stagnation temperature $T_{\text{SST,max}}$ increases (Fig. 18b). SRI* reference coatings thus cover a wider temperature range in comparison to SRI reference coatings and are more appropriate for CSP applications.

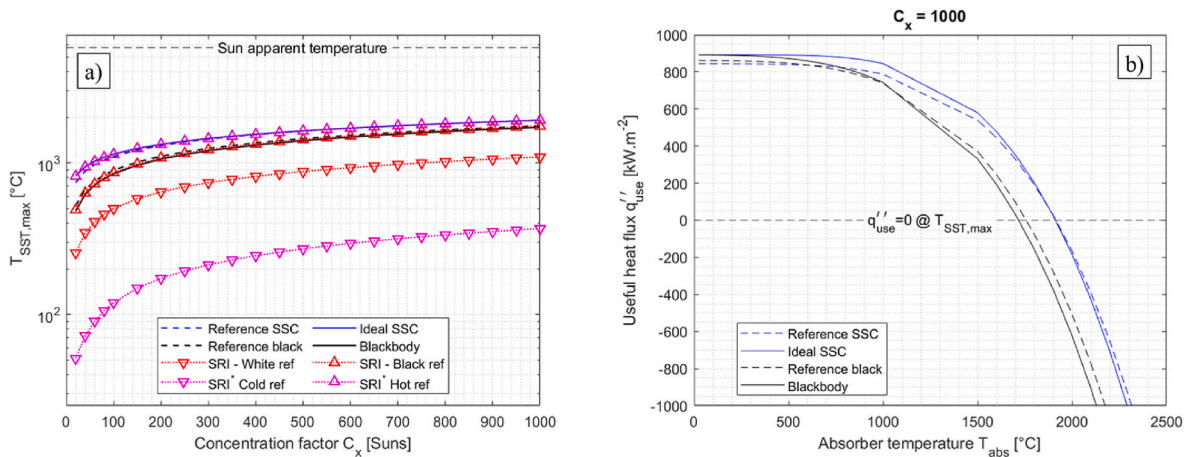


Fig. 16. Calculation of $T_{\text{SST,max}}$ a) as a function of C_x for all reference coatings. b) Calculation at $C_x = 1000$ for reference STAC, sweeping the T_{abs} parameter beyond the reference coating operating temperature range.

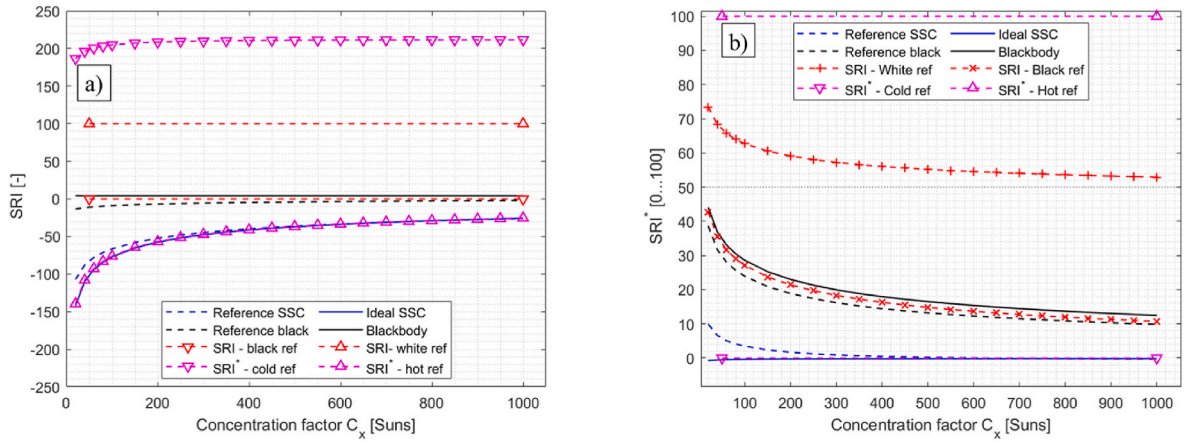


Fig. 17. Calculation of solar reflectance indices as a function of C_x . a) SRI b) SRI*.

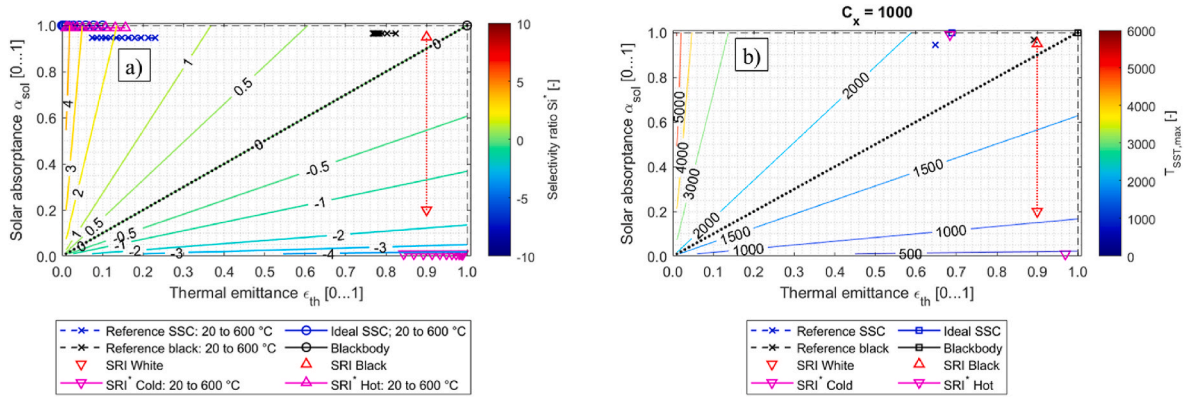


Fig. 18. a) Si^* as a function of α_{sol} and ϵ_{th} . b) $T_{SST,max}$ as a function of α_{sol} and ϵ_{th} for $C_x = 1000$.

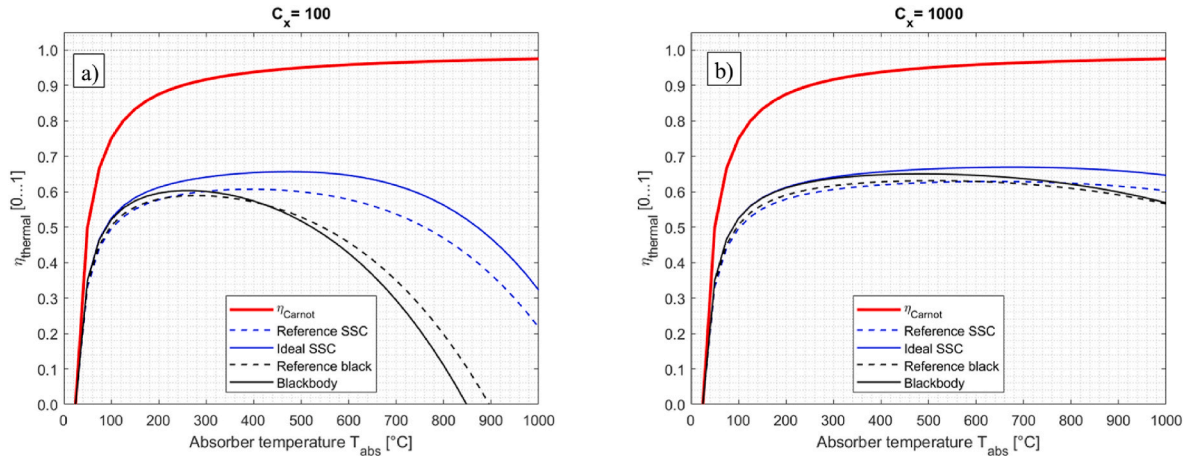


Fig. 19. Thermal efficiency $\eta_{thermal}$ for STAC with $f_{Carnot} = 70\%$ a) at $C_x = 100$ suns b) at $C_x = 1000$ suns.

4.3.3. Thermal efficiency and peak efficiency temperature

The thermal efficiency $\eta_{thermal}$ (Eq.(31) and (32)) is calculated for reference STAC as a function of T_{abs} , at $C_x = 100$ (Fig. 19a) and $C_x = 1000$ in (Fig. 19b), including Carnot efficiency η_{Carnot} (Eq. (30)) as an upper limit. This representation offers a global perspective for the comparison of STAC performance: the thermal efficiency curve increases steeply from 0% at 25 °C above ~50% at 100 °C, it reaches a maximum plateau and it then drops down to 0% at $T_{SST,max}$. The length of the plateau indicates the optimal operating temperature range for a given

concentration factor C_x .

In Fig. 19, the ideal SSC reaches the maximal $\eta_{thermal}$ value among STAC for any temperature. At $C_x = 100$ (Fig. 19a), the ideal blackbody ranks second up to 300 °C, while the reference SSC and black coating are on par up to 300 °C. Above 300 °C, the reference SSC then ranks second, while black coatings drop in thermal efficiency $\eta_{thermal}$ until they achieve $T_{SST,max}$. Both SSCs exhibit a wider plateau at maximal efficiency, from ~300 to 600 °C for the ideal SSC and from ~250 to 450 °C for the real SSC. These temperature ranges are compatible with the PTC

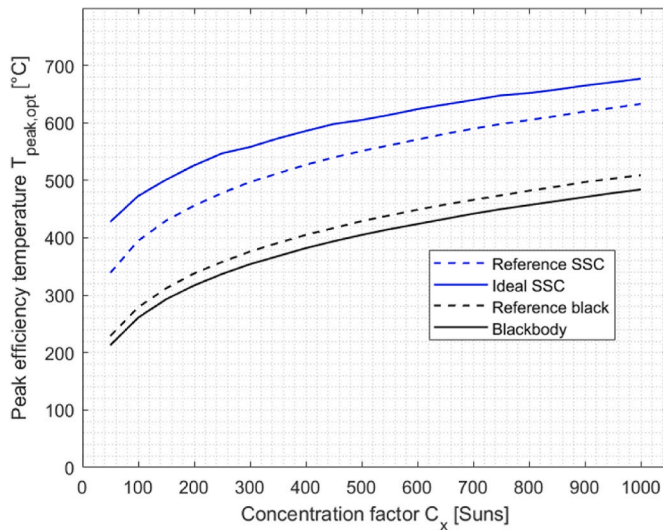


Fig. 20. Peak efficiency temperature $T_{peak,opt}$ as a function of C_x for reference STAC.

application. For this configuration, a selecting a SSC is thus more efficient than a black coating, as discussed previously in subsection 4.2.3.

At $C_x = 1000$ suns, the ranking is different: the ideal blackbody (black line) ranks second up to ~ 800 °C. The reference black coating (black dotted line) ranks third up to 600 °C. The reference SSC (blue dotted line) respectively surpasses the reference black coating at 600 °C and the ideal blackbody at 800 °C. A wide plateau is observed for the reference SSC and black coating, from ~ 300 to 650 °C. As discussed in Subsection 4.2.3, black coatings perform quite well in these conditions for a wide temperature range, compatible with the CRS application.

The peak efficiency temperature $T_{peak,opt}$ (Eq. (30)) is plotted for all STAC in Fig. 20 as a function of C_x . This plot confirms the observation that a SSC (blue lines) reach its optimal $\eta_{thermal}$ value at a higher temperature than a black coating (black lines). The ranking is consistent with (Fig. 16) for the $T_{SST,max}$ FoM: the ideal SSC ranks first (blue line), the reference SSC second (blue dotted line), the reference black coating third (black dotted line) and the ideal blackbody fourth (black line). A SSC thus allows operating efficiently at higher temperature level than a black coating, for any C_x value.

The current definition of $\eta_{thermal}$ neglects the temperature drop across the STAC and metal substrate (Fig. 2), as the heat transfer from the STAC to the HTF is not modelled in this paper. Assuming a thin film SSC ($\ll 1$ μm) with high thermal conductivity (~ 10 $\text{W m}^{-1} \text{K}^{-1}$), the temperature drop across the STAC can be neglected ($\Delta T \ll 1$ K). However, for a sprayable ceramic black coating (~ 40 μm), and a low thermal conductivity of (~ 1 $\text{W m}^{-1} \text{K}^{-1}$), the temperature drop across the STAC should not be negligible ($\Delta T \sim 10$ K) and the coating would then act as a Thermal Barrier Coating (TBC) [148]. The lack of experimental thermal conductivity data for STAC at operating temperature does not yet allow for an accurate correction for this effect.

4.4. Summary and discussion

To summarize our comparative analysis of FoMs, references STAC (Section 2.3) are evaluated and ranked in Table 7 for opto-thermal FoMs listed in Table 3 and analyzed in this paper.

The four reference coatings are divided into two subgroups, i.e. two black coatings on the one hand and two SSCs on the other hand. Black coatings respectively exhibit high α_{sol} and ϵ_{th} values ($\alpha_{sol} > 95\%$, $\epsilon_{th} > 80\%$), while SSC exhibit a high α_{sol} and a low ϵ_{th} values ($\alpha_{sol} > 95\%$, $\epsilon_{th} < 80\%$). Both reference FoMs are coupled, as there exists an overlap between solar and blackbody spectral irradiance (Fig. 8). Compound FoMs allow a finer ranking of STAC based on their opto-thermal performance.

Any SSC can be characterized in first approximation by a simple spectral model $f_{SSC}(\lambda)$, parameterized with a few spectral FoMs, i.e. a cut-off wavelength $\lambda_{cut-off}$, a shape factor f_{shape} and asymptotical reflectance values ρ_{low} and ρ_{high} . This spectral model is however not suitable for black coatings. The goodness of fit of such spectral models thus allow discriminating between SSCs and black coatings.

Some FoMs allow a categorical discrimination of our reference STAC into two subgroups, i.e. black coating and SSC, while being applicable for any coating. These FoMs are namely the selective index Si, the maximum steady-state temperature $T_{SST,max}$ and the solar reflectance index SRI (Fig. 18). These FoMs do not require a detailed knowledge of spectral features. Two of these FoMs (Si and SRI) have been tentatively renormalized (Si^* and SRI^*). Si^* is a logarithmic transformation of Si, to re-scale its range. Boundary conditions and reference coatings are updated for SRI^* to correct shortcomings of the SRI. The SRI and SRI^* calculations both rely on a theoretical FoM, i.e. $T_{SST,max}$. This later FoM typically exceeds the maximal operating temperature allowed for the STAC.

Table 7
Comparison of reference STAC for different opto-thermal FoMs.

Level	FoM	Optimization Target	Reference SSC	Ideal SSC	Reference black	Blackbody
1	α_{sol} (AM1.5 d)	Max	94.6% (4th)	100% (1st)	96.6% (3rd)	100% (1st)
	$\epsilon_{th,calc}$ (T_{abs}) ($100 < T_{abs} < 1000$ °C)	Min	10 \rightarrow 40% (2nd)	0 \rightarrow 30% (1st)	77 \rightarrow 83% (3rd)	100% (4th)
1	$f_{SSC}(\lambda)$	Min (RMSE)	Logistic model	Unit step function	N.A.	Constant
	$\lambda_{cut-off}$	≤ 2.5 μm	~ 2.4	2.5		$\rightarrow +\infty$
	f_{shape}	Max	~ 7	$\rightarrow +\infty$		$\rightarrow 0$
	Asymptote 1: ρ_{low}	Min	~ 0.018	0		$\rightarrow 0$
	Asymptote 2: ρ_{high}	Max	~ 0.972	1		$\rightarrow 0$
2	Si ($100 < T_{abs} < 1000$ °C)	Max	10.9 \rightarrow 2.5 (2nd)	$6.10^3 \rightarrow \sim 3$ (1st)	1.16 \rightarrow 1.25 (3rd)	1 (4th)
	Si^* ($100 < T_{abs} < 1000$ °C)	Max	2.4 \rightarrow 0.9 (2nd)	8.7 \rightarrow 1.15 (1st)	0.15 \rightarrow 0.23 (3rd)	0 (4th)
	q_{use}''	Max	Dynamic ranking (Pareto fronts)			
	η_{opt-th}	Max	Ideal SSC always ranked first			
	$Z_{trade-off}$	[–]	Reference SSC more efficient for low values (< 30) Reference black coating favored for high values (> 30)			
3	$T_{SST,max}$ ($20 < C_x < 1000$)	Max	740 \rightarrow 1915 °C	820 \rightarrow 1920 °C	520 \rightarrow 1760 °C	480 \rightarrow 1720 °C
	SRI ($20 < C_x < 1000$)	Min	$-110 \rightarrow -26$ (2nd)	$-140 \rightarrow -26$ (1st)	$-13 \rightarrow -2$ (3rd)	~ 4 (4th)
	SRI^* ($20 < C_x < 1000$)	Min	10 \rightarrow -0.3 (2nd)	$-0.75 \rightarrow -0.1$ (1st)	39 \rightarrow 10 (3rd)	44 \rightarrow 13 (4th)
	$\eta_{thermal}$ ($20 < C_x < 1000$)	Max	Dynamic ranking (Pareto fronts) Ideal SSC always ranked first			
	$T_{peak,opt}$ ($20 < C_x < 1000$)	Max	2nd	1st	3rd	4th

Other FoMs, i.e. \dot{q}_{use}'' , η_{opt-th} , $\eta_{thermal}$, allow a dynamic ranking depending on the operating point $\{C_x; T_{abs}\}$. These FoMs are directly related to the STAC opto-thermal efficiency. The dynamic ranking among STAC is a function of the trade-off FoM, i.e. $Z_{trade-off}$. For these three FoMs, the ideal SSC always ranked first in the considered operating range [C_x : 20 ... 1000 °C; T_{abs} : 25 ... 1000 °C]. Different cases could be identified: i) for a “low” C_x and a “high” T_{abs} , the solar absorptance α_{sol} is dominant over the thermal emittance ε_{th} . It is thus preferable to maximize α_{sol} (black coating) before minimizing ε_{th} (SSC); ii) for a “high” C_x and a “low” T_{abs} , α_{sol} has a lower weight and it thus clearly relevant to minimize ε_{th} , and thus select a SSC, for instance in PTC applications; iii) for intermediate operating ranges, a Pareto front could be identified, where both the reference black coating and SSC perform equally well. (Fig. 13). The Pareto front for \dot{q}_{use}'' and η_{opt-th} could be also analyzed from a spectral perspective (Fig. 14), to better understand at which wavelength the ranking among STAC may evolve, before reaching an asymptotical value.

However, by definition, \dot{q}_{use}'' and η_{opt-th} monotonously decrease at higher absorber temperature T_{abs} . This is not the case for $\eta_{thermal}$, which reach an optimum at the peak efficiency temperature $T_{peak,opt}$, before dropping to zero at $T_{SST,max}$ ($T_{peak,opt} \ll T_{SST,max}$). The FoM η_{opt-th} offers a more realistic perspective of the system efficiency and the FoM $T_{peak,opt}$ indicates the optimal temperature range for the STAC operation.

The FoM set analyzed in this review offer a complementarity perspective for ranking different STAC formulations, while the methodological framework is also applicable for solar selective reflective materials [141,142,149,150].

5. Conclusion

In this review, opto-thermal Figures of merit relevant for the characterization of Solar Thermal Absorber Coatings were analyzed and compared. These figures of merit were calculated on the basis of spectral measurements (0.25–20 μm) made at room temperature for a near-normal angle of incidence. Reference solar thermal absorber coatings included two types of coatings, i.e. solar selective and black coatings. For each coating type, a reference coating and an ideal coating were analyzed.

For the comparative analysis, a set of modelling assumptions were made for simplification, in particular a flat geometry, negligible angular effects, negligible convection and stable optical properties at operating temperature. The list of figures of merit includes two standard indicators, i.e. solar absorptance α_{sol} and thermal emittance ε_{th} , spectral parameters for a solar selective coating model ($f_{SSC}(\lambda)$), i.e. cut-off wavelength ($\lambda_{cut-off}$), shape factor (f_{shape}) and reflectivity asymptotes (ρ_{low} and ρ_{high}). Further existing compound figures of merit were analyzed, i.e. Selectivity ratio Si , useful heat flux \dot{q}_{use}'' , opto-thermal efficiency η_{opt-th} , Maximum steady-state temperature $T_{SST,max}$, Solar reflectance index SRI and thermal efficiency $\eta_{thermal}$. Additional figures of merit were introduced, i.e. a normalized selectivity ratio Si^* and solar reflectance index SRI^* , a trade-off factor $Z_{trade-off}$ and a peak efficiency temperature $T_{peak,opt}$. The interactions between all figures of merit were summarized in a synoptical diagram.

A first subset of figures of merit allows a finer characterization of selectivity, i.e. spectral model parameters $\{\lambda_{cut-off}, f_{shape}, \rho_{low}$ and $\rho_{high}\}$, the selectivity ratio Si , the maximum steady-state temperature $T_{SST,max}$ and the solar reflectance index SRI. Si and SRI figures of merit have been tentatively normalized (Si^* and SRI^*) for a better adaptation in the field of CSP. Their correlation to the absorber temperature T_{abs} and the maximum steady-state temperature $T_{SST,max}$ has also been highlighted.

A second subset of figures of merit, i.e. useful heat flux \dot{q}_{use}'' , opto-thermal efficiency η_{opt-th} and thermal efficiency $\eta_{thermal}$ allow a dynamic ranking of solar thermal absorber coatings, depending on the specific operating point $\{C_x; T_{abs}\}$ and the corresponding trade-off factor $Z_{trade-off}$ between solar absorptance α_{sol} and thermal emittance ε_{th} . The

existence of a Pareto front between a reference black coating and a reference solar selective coating has been shown and a spectral evolution of cumulative opto-thermal efficiency has also been illustrated. At high concentration and low temperature, the influence of solar absorptance is dominant over thermal emittance, favoring black coatings for central receiver systems. Spectral selectivity is more important to achieve at lower concentration and higher temperature, for instance in parabolic trough applications.

Thermal efficiency $\eta_{thermal}$ corrects a shortcoming of the opto-thermal efficiency η_{opt-th} which decreases at higher temperature by definition, while a higher temperature is desired to maximize the thermal efficiency. Thermal efficiency $\eta_{thermal}$ offers the most comprehensive perspective: it increases up to a plateau around the peak efficiency temperature $T_{peak,opt}$, then it then decreases until the maximum steady-state temperature $T_{SST,max}$. The peak efficiency temperature $T_{peak,opt}$ is deemed more relevant as the maximum steady-state temperature $T_{SST,max}$, as the peak efficiency temperature $T_{peak,opt}$ indicates the optimal operating temperature range of a solar thermal absorber coating, while the maximum steady-state temperature $T_{SST,max}$ typically exceeds the maximal operating temperature of such coatings.

Further research is conducted within the EU project SFERA-III to verify whether spectral properties measured at room temperature for oxidized substrates and black coatings are stable at higher temperature up to 800 °C, without compromising the coating durability. These measurements have on the one hand a potential impact on the calculation of α_{sol} and ε_{th} , if any spectral shift is detected. On the other hand, potential spectral shifts at higher temperature may also affect infrared temperature measurements, requiring a new method for retrieving the effective band emissivity and calibrating in situ the infrared thermography setup.

Credit author statement

Simon Caron: Conceptualization, Methodology, Validation, Investigation, Visualization, Writing -Original draft, Review & Editing. Jorge Garrido: Conceptualization, Methodology, Validation, Investigation, Visualization, Writing - Original draft, Review & Editing. Jesus Balles-trin: Writing – Review and Editing. Florian Sutter: Writing – Review and Editing, Project administration, Funding acquisition. Marc Röger: Writing – Review and Editing, Project administration, Funding acquisition. Francisco Manzano-Agugliaro: Writing – Review and Editing, Visualization, Supervision.

Declaration of competing interest

The authors declare that they have no known competing financial interests or personal relationships that could have appeared to influence the work reported in this paper.

Acknowledgments

This project (EU SFERA-III) has received funding from the European Union's Horizon 2020 Research and Innovation Program under grant agreement n° 823802. We thank both Dr. Christina Hildebrandt (Fraunhofer Institut for Solar Energy Systems) and Yaniv Binyamin (Brightsource Industries) for supplying reference solar thermal absorber coated samples within the EU-Raiselife project (Horizon 2020, Contract n686008).

References

- [1] Wiesenfarth M, Philipps SP, Bett AW, Horowitz K, Kurtz K. Current Status of Concentrator Photovoltaic (CPV) Technology. Version 1.3. 2017. accessed 15/05/21, <https://www.ise.fraunhofer.de/content/dam/ise/de/documents/publications/studies/cpv-report-ise-nrel.pdf>.

- [2] Xie WT, Dai YJ, Wang RZ, Sumathy K. Concentrated solar energy applications using Fresnel lenses: a review. *Renew Sustain Energy Rev* 2011;15(6):2588–606. <https://doi.org/10.1016/j.rser.2011.03.031>.
- [3] Sundarraj P, Maity D, Roy SS, Taylor RA. Recent advances in thermoelectric materials and solar thermoelectric generators – a critical review. *RSC Adv* 2014;4:46860–74. <https://doi.org/10.1039/C4RA05322B>.
- [4] Champier D. Thermoelectric generators: a review of applications. *Energy Convers Manag* 2017;140:167–81. <https://doi.org/10.1016/j.enconman.2017.02.070>.
- [5] Kraemer D, Jie Q, McEnaney K, Cao F, Liu W, Weinstein LA, Loomis J, Ren Z, Chen G. Concentrating solar thermoelectric generators with peak efficiency of 7.4. *Nat. Energy* 2016;1(8 pages):16153. <https://doi.org/10.1038/energy.2016.153>.
- [6] Fernandez-Garcia A, Zarza E, Valenzuela L, Perez M. Parabolic-trough solar collectors and their applications. *Renew Sustain Energy Rev* 2010;14(7):1695–721. <https://doi.org/10.1016/j.rser.2010.03.012>.
- [7] Manikandan GK, Iniyas S, Goic R. Enhancing the optical and thermal efficiency of a parabolic trough collector – a review. *Appl Energy* 2019;235(1):1524–40. <https://doi.org/10.1016/j.apenergy.2018.11.048>.
- [8] Frederiksson J, Eickhoff M, Giese L, Herzog M. A comparison and evaluation of innovative parabolic trough collector concepts for large-scale application. *Sol Energy* 2021;215:266–310. <https://doi.org/10.1016/j.solener.2020.12.017>.
- [9] Zhu G, Wendelin T, Wagner MJ, Kutscher C. History, Current State, and future of linear Fresnel concentrating solar collectors. *Sol Energy* 2014;103:69–652. <https://doi.org/10.1016/j.solener.2013.05.021>.
- [10] Morin G, Dersch J, Platzer W, Eck M, Häberle A. Comparison of linear Fresnel and parabolic trough collector power plants. *Sol Energy* 2012;86(1):1–12. <https://doi.org/10.1016/j.solener.2011.06.020>.
- [11] Ho CK, Iverson BD. Review of high-temperature central receiver designs for concentrated solar power. *Renew Sustain Energy Rev* 2014;29:835–46. <https://doi.org/10.1016/j.rser.2013.08.099>.
- [12] Ho CK. Advances in central receivers for concentrating solar applications. *Sol Energy* 2017;152:38–56. <https://doi.org/10.1016/j.solener.2017.03.048>.
- [13] Li L, Coventry J, Bader R, Pye J, Lipinski W. Optics of solar central receiver systems: a review. *Opt Express* 2016;24(14):A985–1007. <https://doi.org/10.1364/OE.24.00A985>.
- [14] Rizvi AA, Danish SN, El-Leathy A, Al-Ansary H, Yang D. A review and classification of layouts and optimization techniques used in design of heliostat fields in solar central receiver systems. *Sol Energy* 2021;218:296–311. <https://doi.org/10.1016/j.solener.2021.02.011>.
- [15] Coventry J, Andracka C, Dish Systems for Csp. *Sol Energy* 2017;152:140–70. <https://doi.org/10.1016/j.solener.2017.02.056>.
- [16] Zayed ME, Zhao J, Elsheikh AH, Li W, Sadek S, Aboelmaaref MM. A comprehensive review on Dish/Stirling concentrated solar power systems: design, optical and geometrical analyses, thermal performance assessment and applications. *J Clean Prod* 2021;283:124664. <https://doi.org/10.1016/j.jclepro.2020.124664>.
- [17] Imenes AG, Mills DR. Spectral beam splitting technology for increased conversion efficiency in solar concentrating systems: a review. *Sol Energy Mater Sol Cell* 2004;84(1–4):19–69. <https://doi.org/10.1016/j.solmat.2004.01.038>.
- [18] Mojiri A, Taylor R, Thomsen E, Rosengarten G. Spectral beam splitting for efficient conversion of solar energy – a review. *Renew Sustain Energy Rev* 2013;28:654–63. <https://doi.org/10.1016/j.rser.2013.08.026>.
- [19] Liang H, Wang F, Yang L, Cheng Z, Shuai Y, Tan H. Progress in full spectrum solar energy utilization by spectral beam splitting hybrid PV/T system. *Renew Sustain Energy Rev* 2021;141:119785. <https://doi.org/10.1016/j.rser.2021.110785>.
- [20] Royne A, Dey CJ, Mills R. Cooling of photovoltaic cells under concentrated illumination: a critical review. *Sol Energy Mater Sol Cell* 2005;86(4):451–83. <https://doi.org/10.1016/j.solmat.2004.09.003>.
- [21] Hasan A, Sawar J, Shah AH. Concentrated photovoltaic: a review of thermal aspects, challenges and opportunities. *Renew Sustain Energy Rev* 2018;94:835–52. <https://doi.org/10.1016/j.rser.2018.06.014>.
- [22] Lilliestam J, Pitz-Paal R. Concentrating solar power for less than USD 0.07 per kWh : finally the breakthrough. *Renew. Energy Focus* 2018;26:17–21. <https://doi.org/10.1016/j.ref.2018.06.002>.
- [23] Schöninger F, Thonig R, Resch G, Lilliestam J. Making the sun shine at night: comparing the cost of dispatchable concentrating solar power and photovoltaics with storage. *Energy Sources B Energy Econ Plann* 2021;16(1):55–74. <https://doi.org/10.1080/15567249.2020.1843565>.
- [24] Forristall R. Heat transfer analysis and modelling of a parabolic trough solar receiver implemented in Engineering Equation Solver. National Renewable Energy Laboratory Technical Report; 2003. <https://doi.org/10.2172/15004820>. NREL/TP-550-34169.
- [25] Kalogirou SA. A detailed thermal model of a parabolic trough collector receiver. *Energy* 2012;48(1):298–306. <https://doi.org/10.1016/j.energy.2012.06.023>.
- [26] Bradshaw RW, Dawson DB, De La Rosa W, Gilbert R, Goods SH, Hale MJ, Jacobs P, Jones SA, Kolb GJ, Pacheco JE, Prairie MR, Reilly HE, Showalter SK, Vant-Hull LL. Final Test and Evaluation Results from the Solar Two Project. 2002. <https://doi.org/10.2172/793226>. Sandia National Laboratories, Technical Report SAND2002-0120.
- [27] Litwin RZ, Pacheco JE. Receiver System: Lessons Learned from Solar Two. 2002. <https://doi.org/10.2172/800776>. Sandia National Laboratories, Technical Report SAND2002-0084.
- [28] Kennedy CE. Review of Mid- to High-Temperature Solar Selective Absorber Materials. National Renewable Energy Laboratory Technical Report; 2002. <https://doi.org/10.2172/15000706>. NREL/TP-520-31267.
- [29] Xu K, Du M, Hao L, Mi J, Yu Q, Li S. A review of high-temperature selective absorber coatings for solar thermal applications. *J. Materiomc* 2020;6(1):167–82. <https://doi.org/10.1016/j.jmat.2019.12.012>.
- [30] Ho CK, Mahoney AR, Ambrosini A, Bencomo M, Hall A, Lambert TN. Characterization of pyromark 2500 paint for high-temperature solar receivers. *J Sol Energy Eng* 2014;136(1). <https://doi.org/10.1115/1.4024031>. 014502 (4 pages).
- [31] Coventry J, Burge P. Optical properties of Pyromark 2500 coatings of variable thicknesses on a range of materials for concentrating solar thermal applications. *AIP Conf. Proc.* 2017;1850. <https://doi.org/10.1063/1.4984355>. 030012 (8 pages).
- [32] Ambrosini A, Boubault A, Ho CK, Banh L, Lewis JR. Influence of application parameters on stability of Pyromark® 2500 receiver coatings. *AIP Conf. Proc.* 2019;2126. <https://doi.org/10.1063/1.5117514>. 030002 (8 pages).
- [33] Benoit H, Spreafico L, Gauthier D, Flamant G. Review of heat transfer fluids in tube-receivers in concentrating solar thermal systems: properties and heat transfer coefficients. *Renew Sustain Energy Rev* 2016;55:298–315. <https://doi.org/10.1016/j.rser.2015.10.059>.
- [34] Lorenzin N, Abanades A. A review on the application of liquid metals as heat transfer fluid in Concentrated Solar Power technologies. *Int J Hydrogen Energy* 2016;41(17):6990–5. <https://doi.org/10.1016/j.ijhydene.2016.01.030>.
- [35] Zhang K, Hao L, Du M, Mi J, Wang JN, Meng JP. A review on thermal stability and high temperature induced ageing mechanisms of solar absorber coatings. *Renew Sustain Energy Rev* 2017;67:1282–99. <https://doi.org/10.1016/j.rser.2016.09.083>.
- [36] Boubault A, Ho CK, Hall A, Lambert TN, Ambrosini A. Durability of solar absorber coatings and their cost-effectiveness. *Sol Energy Mater Sol Cell* 2017;166:176–84. <https://doi.org/10.1016/j.solmat.2017.03.010>.
- [37] Noë L, Sest E, Kapun G, Ruiz-Zepeda F, Binyamin Y, Merzel F, Jerman I. High-solar-absorptance CSP coating characterization and reliability testing with isothermal cyclic loads for service-life prediction. *Energy Environ Sci* 2019;12:1679–94. <https://doi.org/10.1039/C8EE03536A>.
- [38] Ho CK, Pacheco JE. Levelized Cost of Coating (LCOCC) for selective absorber materials. *Sol Energy* 2014;108:315–21. <https://doi.org/10.1016/j.solener.2014.05.017>.
- [39] Boubault A, Ho CK, Hall A, Lambert TN, Ambrosini A. Levelized cost of energy (LCOE) metric to characterize solar absorber coatings for the CSP industry. *Renew Energy* 2016;85:472–83. <https://doi.org/10.1016/j.renene.2015.06.059>.
- [40] Moens L, Blake DM. Advanced heat transfer and thermal storage fluids. In: Proceedings of the ASME 2005 International Solar Energy Conference; 2005. p. 791–3. <https://doi.org/10.1115/ISEC2005-76192>. ISEC2005-76192.
- [41] Moens L, Blake DM. Mechanisms of hydrogen formation in solar parabolic trough receivers. *J Sol Energy Eng* 2010;132(3). <https://doi.org/10.1115/1.4001402>. 0410006 (5 pages).
- [42] Jung C, Dersch J, Nietsch A, Senholdt M. Technological perspectives of silicon heat transfer fluids for Concentrated Solar Power. *Energy Procedia* 2015;69:663–71. <https://doi.org/10.1016/j.egypro.2015.03.076>.
- [43] Jung C, Senholdt M. Comparative study on hydrogen issues of Biphenyl/Diphenyl oxide and polydimethylsiloxane heat transfer fluids. *AIP Conf. Proc.* 2020;2303:150009. <https://doi.org/10.1063/5.0028894>. 10 pages.
- [44] Bonk A, Sau S, Uranga M, Hernaiz M, Bauer T. Advanced heat transfer fluids for direct molten salt line-focusing CSP plants. *Prog Energy Combust Sci* 2018;67:69–87. <https://doi.org/10.1016/j.peccs.2018.02.002>.
- [45] Bonk A, Braun M, Sözt VA, Bauer T. Solar Salt – pushing an old material for energy storage to a new limit. *Appl Energy* 2020;262(15):114535. <https://doi.org/10.1016/j.apenergy.2020.114535>. 7 pages.
- [46] Zhu G, Libby C. Review and future perspective of central receiver design and performance. *AIP Conf. Proc.* 2017;1850:030052. <https://doi.org/10.1063/1.4984395>. 8 pages.
- [47] Prieto C, Fereres S, Ruiz-Cabañas FJ, Rodriguez- Sanchez A, Montero C. Carbonate molten salt solar thermal pilot facility: plant design, commissioning and operation up to 700 °C. *Renew Energy* 2020;151:528–41. <https://doi.org/10.1016/j.renene.2019.11.045>.
- [48] Ding W, Bauer T. Progress in research and development of molten chloride salt technology for next generation concentrated solar power plants. *Engineering* 2021;7(3):334–47. <https://doi.org/10.1016/j.eng.2020.06.027>.
- [49] Coventry J, Andracka C, Pye J, Blanco M, Fisher J. A review of sodium receiver technologies for central receiver solar power plants. *Sol Energy* 2015;122:749–62. <https://doi.org/10.1016/j.solener.2015.09.023>.
- [50] Fritsch A, Frantz C, Uhlig R. Techno-economic analysis of solar thermal power plants using liquid sodium as heat transfer fluid. *Sol Energy* 2019;177:155–62. <https://doi.org/10.1016/j.solener.2018.10.005>.
- [51] Calderon A, Barreneche C, Palacios A, Segarra M, Prieto C, Rodriguez-Sanchez A, Fernandez AI. Review of solid particle materials for heat transfer fluid and thermal energy storage in solar thermal power plants. *Energy Storage* 2019;1(4):1–20. <https://doi.org/10.1002/est2.63>.
- [52] Galiullin T, Gobereit B, Naumenko D, Buck R, Amsbeck L, Neises-von Puttkamer M, Quadakkers WJ. High temperature oxidation and erosion of candidate materials for particle receivers of concentrated solar power tower systems. *Sol Energy* 2019;188:883–9. <https://doi.org/10.1016/j.solener.2019.06.057>.
- [53] Gobereit B, Amsbeck L, Happich C, Schmücker M. Assessment and improvement of optical properties of particles for solid particle receiver. *Sol Energy* 2020;199:844–51. <https://doi.org/10.1016/j.solener.2020.02.076>.
- [54] Gimeno-Furio A, Hernandez L, Martinez-Cuenca R, Mondragon R, Vela A, Cabedo L, Barreneche C, Jacob M. New coloured coatings to enhance silica sand

- absorbance for direct particle solar receiver applications. *Renew Energy* 2020; 152:1–8. <https://doi.org/10.1016/j.renene.2020.01.053>.
- [55] Zhao W, Sun Z, Alwahabi ZT. Emissivity and absorption function measurements of Al₂O₃ and SiC particles at elevated temperature for the utilization in concentrated solar receivers. *Sol Energy* 2020;207:183–91. <https://doi.org/10.1016/j.solener.2020.06.079>.
 - [56] Navarro Hermoso JL, Espinosa-Rueda G, Heras C, Salinas I, Martínez N, Gallas M. Parabolic trough solar receiver characterization using specific test bench for transmittance, absorbance and heat loss simultaneous measurement. *Sol Energy* 2016;136:268–77. <https://doi.org/10.1016/j.solener.2016.07.012>.
 - [57] Espinosa-Rueda G, Navarro Hermoso JL, Martínez-Sanz N, Gallas-Torreira M. Vacuum evaluation of parabolic trough receiver tubes in a 50 MW concentrated solar power plant. *Sol Energy* 2016;139:36–46. <https://doi.org/10.1016/j.solener.2016.09.017>.
 - [58] Raccurt O, Matino F, Disdier A, Brailion J, Stollo A, Bourdon D, Maccari A. In air durability study of solar selective coating for parabolic trough technology. *AIP Conf. Proc.* 2017;1850:130010. <https://doi.org/10.1063/1.4984504>. 8 pages.
 - [59] Röger M, Lüpfer E, Caron S, Dieckmann S. Techno-economic analysis of receiver replacement scenarios in a parabolic trough field. *AIP Conf. Proc.* 2016;1734. <https://doi.org/10.1063/1.4949082>. 040030 (11 pages).
 - [60] Zoschke T, Frantz C, Schöttl P, Fluri T, Uhlig R. Techno-economic assessment of new material developments in central receiver solar power plants. *AIP Conf. Proc.* 2019;2126. <https://doi.org/10.1063/1.5117580>. 030068 (8 pages).
 - [61] Tsuda K, Murakami Y, Torres JF, Coventry J. Development of high absorption, high durability coatings for solar receivers in CSP plants. *AIP Conf. Proc.* 2018; 2033. <https://doi.org/10.1063/1.5067075>. 040039 (8 pages).
 - [62] Harzallah R, Larnicol M, Leclercq C, Herbein A, Campana F. Development of high performances solar absorber coatings. *AIP Conf. Proc.* 2019;2126. <https://doi.org/10.1063/1.5117538>. 030026 (11 pages).
 - [63] Jerman I, Zepeda FR, Merzel F, Noë L. High-temperature “ion baseball” for enhancing concentrated solar power efficiency. *Sol Energy Mater Sol Cell* 2019; 200:109974. <https://doi.org/10.1016/j.solmat.2019.109974>. 12 pages.
 - [64] Selvakumar N, Barshilia HC. Review of physical vapor deposited (PVD) spectrally selective coatings for mid- and high-temperature solar thermal applications. *Sol Energy Mater Sol Cell* 2012;98:1–23. <https://doi.org/10.1016/j.solmat.2011.10.028>.
 - [65] Joly M, Antonetti Y, Python M, Gonzalez M, Gascou T, Scartezinni JL, Schüler A. Novel black selective coating for tubular solar absorbers based on a sol-gel method. *Sol Energy* 2013;94:233–9. <https://doi.org/10.1016/j.solener.2013.05.009>.
 - [66] Cao F, McEnaney K, Chen G, Ren Z. A review of cermet-based spectrally selective solar absorbers. *Energy Environ Sci* 2014;7:1615–27. <https://doi.org/10.1039/C3EE43825B>.
 - [67] Hildebrandt C. High-temperature stable absorber coatings for linear concentrating solar thermal power plants, PhD thesis. Stuttgart University; 2009. <https://doi.org/10.18419/opus-1802>.
 - [68] Heras Pérez I. Multilayer solar selective coatings for high temperature solar applications: from concept to design, PhD thesis. Sevilla University; 2016. <http://hdl.handle.net/11441/47789>.
 - [69] Price H, Forristall R, Wendelin T, Lewandowski A, Moss T, Gummo C. Field Survey of Parabolic Trough Receiver Thermal Performance, ASME 2006 International Solar Energy Conference Proceedings. 2008. p. 109–16. <https://doi.org/10.1115/ISEC2006-99167>. ISEC 2006-99167.
 - [70] Olano X, García de Jalon A, Perez D, Lopez J, Gaston M. Outcomes and features of the inspection of receiver tubes (ITR) system for improved O&M in parabolic trough plants. *AIP Conf. Proc.* 2018;2033. <https://doi.org/10.1063/1.5067027>. 030011 (9 pages).
 - [71] Setien E, Lopez-Martin R, Valenzuela L. Methodology for partial vacuum pressure and heat losses analysis of parabolic troughs receivers by infrared radiometry. *Infrared Phys Technol* 2019;98:341–53. <https://doi.org/10.1016/j.infrared.2019.02.011>.
 - [72] Vant-Hull LL. The role of “allowable flux density” in the design and operation of molten-salt solar central receivers. *J Sol Energy Eng* 2002;124(2):165–9. <https://doi.org/10.1115/1.1464124>.
 - [73] Liao Z, Li X, Xu C, Chang C, Wang Z. Allowable flux density on a solar central receiver. *Renew Energy* 2014;62:747–53. <https://doi.org/10.1016/j.renene.2013.08.044>.
 - [74] Flesch R, Frantz C, Maldonado Quinto D, Schwarzbözl P. Towards an optimal aiming for molten salt power towers. *Sol Energy* 2017;155:1273–81. <https://doi.org/10.1016/j.solener.2017.07.067>.
 - [75] Sanchez-Gonzalez A, Rodriguez-Sanchez MR, Santana D. Aiming strategy model based on allowable flux densities for molten salt central receivers. *Sol Energy* 2017;157:1130–44. <https://doi.org/10.1016/j.solener.2015.12.055>.
 - [76] Sanchez-Gonzalez A, Rodriguez-Sanchez MR, Santana D. Allowable solar flux densities for molten-salt receivers: input to the aiming strategy. *Results Eng.* 2020;5:100074. <https://doi.org/10.1016/j.rineng.2019.100074>. 9 pages.
 - [77] Eitan A, Naor G, Hayut R, Segev I, Golbert J, Pekarsky S, Ziskin A, Medan G, Feigelshtock A, Goldberg N, Kroyzer G. Accurate flux calculations using thermographic IR cameras in concentrated solar power fields. *Quant. InfraRed Thermography (QIRT) Intl. Conf. Proc.* 2014;7. <https://doi.org/10.21611/qirt.2014.220>.
 - [78] InfraTec GmbH, Solar Power Tower Check – Sptc. Solar Power Tower Check - sptc. InfraTec; 2021. accessed 15/05/21.
 - [79] Hernandez D, Olalde G, Gineste JM, Gueymard C. Analysis and experimental results of solar-blind temperature measurements in solar furnaces. *J Sol Energy Eng* 2004;126(1):645–53. <https://doi.org/10.1115/1.1636191>.
 - [80] Marquesado Solar. Andasol 3 solar thermal power plant. 2016. accessed 15/05/21, <https://marquesadosolar.com/foto/solar-field/>.
 - [81] SENER. Gemasolar solar thermal power plant. 2021. accessed 15/05/21, <https://www.energy.sener/projects/gemasolar>.
 - [82] Marquesado Solar. Andasol 3 solar thermal power plant. 2016. accessed 15/05/21, <https://marquesadosolar.com/plant-andasol-3/>.
 - [83] International Organization for Standardization. Solar energy – Collector components and materials – Part 3: Absorber surface durability. ISO 22973-3: 2014 (30 pages). 2014. accessed 15/05/21, <https://www.iso.org/standard/61758.html>.
 - [84] International Organization for Standardization. Space systems – Thermal control coatings for spacecraft – General requirements. ISO 16691:2014 (17 pages). 2014. accessed 15/05/21, <https://www.iso.org/standard/57440.html>.
 - [85] International Organization for Standardization. Space systems – Measurement of thermo-optical properties of thermal control materials. ISO 16378:2013 (36 pages). 2013. accessed 15/05/21, <https://www.iso.org/standard/56558.html>.
 - [86] ASTM International. Standard test method for solar absorbance, reflectance, and transmittance of materials using integrating spheres. ASTM E903; 2020. <https://doi.org/10.1520/E0903-20>. 2020 (17 pages).
 - [87] ASTM International. Standard test method for determination of solar reflectance near ambient temperature using a portable solar reflectometer. 2016. <https://doi.org/10.1520/C1549-16>. ASTM C1549:2016 (6 pages).
 - [88] ASTM International. Standard test method for determination of emittance of materials near room temperature using portable emissometers. 2015. <https://doi.org/10.1520/C1371-15>. ASTM C1371:2015 (8 pages).
 - [89] ASTM International. Standard test methods for total normal emittance of surfaces using inspection-meter techniques. 2019. <https://doi.org/10.1520/E0408-13R19>. ASTM E408:2013 (5 pages).
 - [90] ASTM International. Standard test method for normal spectral emittance at elevated temperatures. 2019. <https://doi.org/10.1520/E0307-72R19>. ASTM E307:1972 (6 pages).
 - [91] ASTM International. Standard test method for total hemispherical emittance of surfaces up to 1400°C. 2020. <https://doi.org/10.1520/C0835-06R20>. ASTM C835:2006 (11 pages).
 - [92] ASTM International. Standard test method for calorimetric determination of hemispherical emittance and the ratio of solar absorbance to hemispherical emittance using solar simulation. 2020. <https://doi.org/10.1520/E0434-10R20>. ASTM E434:2010 (6 pages).
 - [93] Cindrella L. The real utility ranges of the solar selective coatings. *Sol Energy Mater Sol Cell* 2007;91(20):1898–901. <https://doi.org/10.1016/j.solmat.2007.07.006>.
 - [94] Burlafinger K, Vetter A, Barbec CJ. Maximizing concentrated solar power (CSP) plant overall efficiencies by using spectral selective absorbers at optimal operation temperatures. *Sol Energy* 2015;120:428–38. <https://doi.org/10.1016/j.solener.2015.07.023>.
 - [95] Wirz M, Petit J, Haselbacher A, Steinfeld A. Potential improvements in the optical and thermal efficiencies of parabolic trough concentrators. *Sol Energy* 2014;107: 398–414. <https://doi.org/10.1016/j.solener.2014.05.002>.
 - [96] Duffie JA, Beckman WA. Solar engineering of thermal processes. fourth ed. Wiley and Sons; 2013. <https://doi.org/10.1002/9781118671603>.
 - [97] Lovegrove K, Pye J. Concentrating Solar Power Technology: Principles, Developments and Applications. second ed. Woodhead Publishing; 2020. <https://doi.org/10.1016/C2018-0-04978-6>.
 - [98] Caron S, Garrido J, Setien E, Harzallah R, Noë L, Jerman I, Röger M, Sutter F. Forty shades of black: a benchmark of high temperature sprayable black coatings applied on Haynes 230. *AIP Conf. Proc.* 2020;2303:1560007. <https://doi.org/10.1063/5.0028773>. 10 pages.
 - [99] ASTM International. Standard practice for exposure of solar collector cover materials to natural weathering under conditions simulating stagnation mode. 2015. <https://doi.org/10.1520/E881-02R15>. ASTM E881:1992. (8 pages).
 - [100] ASTM International. Standard practice for calculating solar reflectance index of horizontal and low-sloped opaque surfaces. 2019. ASTM E1980:2011 (3 pages, <https://www.astm.org/Standards/E1980.htm>).
 - [101] Muscio A. The solar reflectance index as a tool to forecast the heat released to the urban environment: potentiality and assessment issues. *Climate* 2018;6(1):12. <https://doi.org/10.3390/cli6010012>. 21 pages.
 - [102] Ballestrin J, Marzo A. Solar radiation attenuation in solar tower plants. *Sol Energy* 2012;86(1):388–92. <https://doi.org/10.1016/j.solener.2011.10.010>.
 - [103] Hanrieder N, Wilbert S, Mancera-Guevara D, Buck R, Gualino S, Pitz-Paal R. Atmospheric extinction in solar tower plants – a review. *Sol Energy* 2017;152: 193–207. <https://doi.org/10.1016/j.solener.2017.01.013>.
 - [104] Marzo A, Salmon A, Polo J, Ballestrin J, Soto G, Quiñones G, Alonso-Montesinos J, Carra E, Ibarra M, Cardeil J, Fuentalba E, Escobar R. Solar extinction map in Chile for applications in solar power tower plants, comparison with other places from sunbelt and impact on LCOE. *Renew Energy* 2021;170: 197–211. <https://doi.org/10.1016/j.renene.2021.01.126>.
 - [105] Sutter F, Meyen S, Fernandez-Garcia A, Heller P. Spectral characterization of specular reflectance of solar mirrors. *Sol Energy Mater Sol Cell* 2016;145(3): 248–54. <https://doi.org/10.1016/j.solmat.2015.10.030>.
 - [106] García-Segura A, Fernandez-Garcia A, Arisa MJ, Sutter F, Valenzuela L. Durability studies of solar reflectors: a review. *Renew Sustain Energy Rev* 2016;62:453–67. <https://doi.org/10.1016/j.rser.2015.01.015>.
 - [107] García-Segura A, Sutter F, Martínez-Arcos L, Reche-Navarro TJ, Wiesinger F, Wette J, Buendía-Martínez F, Fernandez-Garcia A. Degradation types of reflector materials used in concentrating solar thermal systems. *Renew Sustain Energy Rev* 2021;143:110879. <https://doi.org/10.1016/j.rser.2021.110879>.

- [108] Sutter F, Montecchi M, von Dahlen H, Fernandez-Garcia A, Röger M. The effect of incidence angle on the reflectance of solar mirrors. *Sol Energy Mater Sol Cell* 2018;176:119–33. <https://doi.org/10.1016/j.solmat.2017.11.029>.
- [109] Paret TW, Wöhrbach M, Buck R, Weinrebe G. Incidence angle on cylindrical receivers of solar power towers. *Sol Energy* 2020;201:1–7. <https://doi.org/10.1016/j.solener.2020.02.077>.
- [110] Kim J, Kim JS, Stein W. Simplified heat loss model for central tower solar receiver. *Sol Energy* 2015;116:314–22. <https://doi.org/10.1016/j.solener.2015.02.022>.
- [111] Hernandez D, Sans JL, Pfänder M. Pyroreflectometry to determine the true temperature and optical properties of surfaces. *J Sol Energy Eng* 2008;130(3). <https://doi.org/10.1115/1.2840575>. 0310003 (4 pages).
- [112] Bitterling M, Bern G, Wilson HR, Heimsath A, Nitz P. Physical models of the bidirectional reflectance of solar receiver coatings. *Sol Energy* 2020;209:653–61. <https://doi.org/10.1016/j.solener.2020.08.054>.
- [113] Macia JD, Herrera-Zamora DM, Lizama-Tzec FI, Bante-Guerra J, Ares-Muzio OE, Oskam G, Romero-Paredes H, Alvarado-Gil JJ, Arancibia-Bulnes C, Ramos-Sanchez V, Villafan-Vidales HI. Optical and thermal properties of selective absorber coatings under CSP conditions. *AIP Conf. Proc.* 2017;1850:120001. <https://doi.org/10.1063/1.4984492>. 8 pages.
- [114] Omt Solution BV. accessed 15/05/2021, <https://omtsolutions.com/>; 2021.
- [115] Labsphere Inc, Technical Guide. Reflectance materials and coatings. 2021. p. 26. accessed 15/05/2021, <https://www.labsphere.com/site/assets/files/2553/a-guide-to-reflectance-materials-and-coatings.pdf>.
- [116] Caron S, Sutter F, Algrer N, Esteller M, Binyamin Y, Baidossi M, Kenigsberg A, Agüero A, Fähsing D, Hildebrandt C. Accelerated ageing of solar receiver coatings: experimental results for T91 and VM12 steel substrates. *AIP Conf. Proc.* 2018;2033:230002. <https://doi.org/10.1063/1.5067230>. 10 pages.
- [117] Caron S, Binyamin Y, Baidossi M, Kenigsberg A, Agüero A, Hildebrandt C, Galet M, Sutter F. Durability testing of solar receiver coatings: experimental results for T91 and VM12 steel substrates. *AIP Conf. Proc.* 2018;2033:230002. <https://doi.org/10.1063/1.5067230>. 10 pages.
- [118] del Campo L, Perez-Saez RB, Esquisabel X, Fernandez I, Tello MJ. New experimental device for infrared spectral directional emissivity measurements in a controlled environment. *Rev Sci Instrum* 2006;77:113111. <https://doi.org/10.1063/1.2393157>. 8 pages.
- [119] Honnerova P, Martan J, Kucera M, Honner M, Hameury J. New experimental device for high-temperature normal spectral emissivity measurement of coatings. *Meas Sci Technol* 2014;25(9). <https://doi.org/10.1088/0957-0233/25/9/095501>. 095501 (9 pages).
- [120] Setien-Fernandez I, Echaniz T, Gonzalez-Fernandez L, Perez-Saez RB, Cespedes E, Sanchez-Garcia JA, Alvarez-Fraga L, Escobar Galindo R, Albella JM, Prieto C, Tello MJ. First spectral emissivity study of a solar selective coating in the 150–600 °C temperature range. *Sol Energy Mater Sol Cell* 2013;117:390–5. <https://doi.org/10.1016/j.solmat.2013.07.002>.
- [121] Echaniz T, Setien-Fernandez I, Perez-Saez RB, Prieto C, Escobar Galindo R, Tello MJ. Importance of the spectral emissivity measurements at working temperature to determine the efficiency of a solar selective coating. *Sol Energy Mater Sol Cell* 2015;140:249–52. <https://doi.org/10.1016/j.solmat.2015.04.009>.
- [122] Gonzalez de Arrieta I, Echaniz T, Fuente R, Rubin E, Chen R, Igartua JM, Tello MJ, Lopez GA. Infrared emissivity of copper-alloyed spinel black coatings for concentrated solar power systems, *Solar Energy Materials and Solar Cells*. *Sol Energy Mater Sol Cell* 2019;200:109961. <https://doi.org/10.1016/j.solmat.2019.109961>. 9 pages.
- [123] Le Baron E, Raccourt O, Giraud P, Adier M, Barriga J, Diaz B, Echegut P, De Sousa Meneses D, Sciti D, Soum-Glaude A, Escape C, Jerman I, Lopez GA, Echaniz T, Tello MJ, Martino F, Maccari A, Mercatelli I, Sani E. Round Robin Test for the comparison of spectral emittance measurement apparatuses. *Sol Energy Mater Sol Cell* 2019;191:476–85. <https://doi.org/10.1016/j.solmat.2018.11.026>.
- [124] ASTM International. Standard Tables for Reference Solar Spectral Irradiances: Direct Normal and Hemispherical on 37° Tilted Surface. 2020. <https://doi.org/10.1520/G0173-03R20>. ASTM G173:2003 (21 pages).
- [125] National Renewable Energy Laboratory, SMARTS. Simple Model of the Atmospheric Radiative Transfer of Sunshine. 2021. accessed 15/05/2021, <https://www.nrel.gov/grid/solar-resource/smarts.html>.
- [126] Gueymard CA. Parameterized transmittance model for direct beam and circumsolar spectral irradiance. *Sol Energy* 2001;71(5):325–46. [https://doi.org/10.1016/S0038-092X\(01\)00054-8](https://doi.org/10.1016/S0038-092X(01)00054-8).
- [127] Gueymard CA, Myers D, Emery K. Proposed reference irradiance spectra for solar energy system testing. *Sol Energy* 2002;73(6):443–67. [https://doi.org/10.1016/S0038-092X\(03\)00005-7](https://doi.org/10.1016/S0038-092X(03)00005-7).
- [128] Jessen W, Wilbert S, Gueymard CA, Polo J, Bian Z, Driesse A, Habte A, Armstrong PR, Vignola F, Ramirez L. Proposal and evaluation of subordinate standard solar irradiance spectra for application in solar energy systems. *Sol Energy* 2018;168:30–43. <https://doi.org/10.1016/j.solener.2018.03.043>.
- [129] Gueymard CA. The sun's total and spectral irradiance for solar energy applications and solar radiation models. *Sol Energy* 2004;76(4):423–53. <https://doi.org/10.1016/j.solener.2003.08.039>.
- [130] Gueymard CA. Revised composite extraterrestrial spectrum based on recent solar irradiance observations. *Sol Energy* 2018;169:434–40. <https://doi.org/10.1016/j.solener.2018.04.067>.
- [131] Optosol GmbH. Absorber control. 2021. accessed 15/05/2021, <http://optosol.com/absorber-control/>.
- [132] Surface Optics Corp. 410-Vis-IR Portable Emissometer & Solar Reflectometer. 2021. accessed 15/05/2021, <https://surfaceoptics.com/products/reflectometers-emissometers/410-vis-ir/>.
- [133] Az Technology. Reflectometers and Emissometers. 2021. accessed 15/05/2021, <http://www.aztechnology.com/products/reflectometers-and-emissometers.html>.
- [134] Devices, Services Company. Emissometer Model AE1 and RD1 Voltmeter. 2021. accessed 15/05/2021, <https://www.devicesandservices.com/AE1%20RD1%20Spec%20Sheet.pdf>.
- [135] Modest MF. Radiative Heat Transfer. third ed. Elsevier; 2013. <https://doi.org/10.1016/C2010-0-65874-3>.
- [136] Howell JR, Pinar Mengüç M, Daun K, Siegel R. Thermal Radiation Heat Transfer. seventh ed. CRC Press, Taylor and Francis Group; 2021, ISBN 9780367347079.
- [137] Santamouris M, Cartalis C, Synnefa A, Kolokotsa D. On the impact of urban heat island and global warming on the power demand and electricity consumption in buildings – a review. *Energy Build* 2015;98:119–24. <https://doi.org/10.1016/j.enbuild.2014.09.052>.
- [138] Santamouris M, Fiorito F. On the impact of the modified urban albedo on ambient temperature and heat related mortality. *Sol Energy* 2021;216:495–507. <https://doi.org/10.1016/j.solener.2021.01.031>.
- [139] Besir AB, Cuce E. Green roofs and facades: a comprehensive review. *Renew Sustain Energy Rev* 2018;82(1):915–39. <https://doi.org/10.1016/j.rser.2017.09.106>.
- [140] Wang C, Wang ZH, Kaloush KE, Shacat J. Cool pavements for urban heat island mitigation: a synthetic review. *Renew Sustain Energy Rev* 2021;146:11171. <https://doi.org/10.1016/j.rser.2021.111171>.
- [141] Farooq AS, Zhang P, Gao Y, Gulfam R. Emerging radiative materials and prospective applications of radiative sky cooling – a review. *Renew Sustain Energy Rev* 2021;144:110910. <https://doi.org/10.1016/j.rser.2021.110910>.
- [142] Libbra A, Muscio A, Siligardi C, Tartarini P. Assessment and improvement of the performance of antisol coatings and surfaces. *Prog Org Coating* 2011;72(1–2): 73–80. <https://doi.org/10.1016/j.porgcoat.2011.02.019>.
- [143] Lehman J, Yung C, Tomlin N, Conklin D, Stephens M. Carbon nanotube-based black coatings. *Appl Phys Rev* 2018;5. <https://doi.org/10.1063/1.5009190>. 011103 (17 pages).
- [144] Acktar Advanced Coatings. World leader in black coatings. 2021. accessed 15/05/2021, <https://www.acktar.com/>.
- [145] Nanosystems Surrey. Vantablack Coating Technology. 2021. accessed 15/05/2021, <https://www.surreynanosystems.com/>.
- [146] Dury MR, Theocharus T, Harrison N, Fox N, Hilton M. Common black coatings – reflectance and ageing characteristics in the 0.32 – 14.3 μm wavelength range. *Opt Commun* 2007;270(2):262–72. <https://doi.org/10.1016/j.optcom.2006.08.038>.
- [147] Jian L, Jian P, Bing H, Xie G. Oxidation kinetics of Haynes 230 alloy in air at temperatures between 650 and 850 °C. *J Power Sources* 2006;159(1):641–5. <https://doi.org/10.1016/j.jpowsour.2005.09.065>.
- [148] Thakare JG, Pandey C, Mahapatra MM, Mulik RS. Thermal Barrier Coatings – a state of the art review. *Met Mater Int* 2020;22. <https://doi.org/10.1007/s12540-020-00705-w>.
- [149] Garrido J, Aichmayer L, Abou-Taouk A, Laumert B. Experimental and numerical performance analyses of Dish-Stirling cavity receivers: radiative property study and design. *Energy* 2019;169:478–88. <https://doi.org/10.1016/j.energy.2018.12.033>.
- [150] Wang W, Mu W, Ye F, Trevisan S, Dutta J, Laumert B. Solar selective reflector materials: another option for enhancing the efficiency of the high-temperature solar receivers/reactors. *Sol Energy Mater Sol Cell* 2021;224:110995. <https://doi.org/10.1016/j.solmat.2021.110995>. 7 pages.